Review of Scientific Instruments

Performance analysis and implementation of a scanning tunneling potentiometry setup: Toward low-noise and high-sensitivity measurements of the electrochemical potential

Cite as: Rev. Sci. Instrum. **92**, 103707 (2021); https://doi.org/10.1063/5.0064341
Submitted: 22 July 2021 • Accepted: 28 September 2021 • Published Online: 15 October 2021

T. Marković, W. Huang, P. Gambardella, et al.

Review of Scientific Instruments | ARTICLE | scitation.org/journal/rsi

Performance analysis and implementation of a scanning tunneling potentiometry setup: Toward low-noise and high-sensitivity measurements of the electrochemical potential

Cite as: Rev. Sci. Instrum. 92, 103707 (2021); doi: 10.1063/5.0064341
Submitted: 22 July 2021 • Accepted: 28 September 2021 •
Published Online: 15 October 2021

View Online Export Citation CrossMark

T. Marković, W. Huang, P. Gambardella, and S. Stepanow[a)]

AFFILIATIONS

Department of Materials, ETH Zurich, 8093 Zurich, Switzerland

[a)]Author to whom correspondence should be addressed: sebastian.stepanow@mat.ethz.ch

ABSTRACT

Scanning tunneling potentiometry allows for studying charge transport on the nanoscale to relate the local electrochemical potential to morphological features of thin films or two-dimensional materials. To resolve the influence of atomic-scale defects on the charge transport, sub-μV sensitivity for the electrochemical potential is required. Here, we present a complete analysis of the noise in scanning tunneling potentiometry for different modes of operation. We discuss the role of various noise sources in the measurements and technical issues for both dc and ac detection schemes. The influence of the feedback controller in the determination of the local electrochemical potential is taken into account. Furthermore, we present a software-based implementation of the potentiometry technique in both dc and ac modes in a commercial scanning tunneling microscopy setup with only the addition of a voltage-controlled current source. We directly compare the ac and dc modes on a model resistor circuit and on epitaxial graphene and draw conclusions on the advantages and disadvantages of each mode. The effects of sample heating and the occurrence of thermal voltages are discussed.

I. INTRODUCTION

The miniaturization of electrical devices in the last few decades[1] has brought their dimensions down to the nm scale where mesoscopic transport properties start playing an important role.[2] However, investigating nanoscale charge transport phenomena is a challenging task.[3,4] Scanning tunneling potentiometry (STP) is a technique capable of measuring the local electrochemical potential (ECP) distribution with μV resolution in current-biased samples, thus providing direct insight into mesoscale electron conduction.[5–11] The ECP is determined by zeroing the tunneling current at the position of the tip via a compensation voltage. This applied compensation voltage is equal to the local ECP since it makes the tip equipotential to the sample right underneath the tip. Simultaneously, the STP technique also maintains the functionality of scanning tunneling microscopy (STM) and, therefore, allows for acquiring the sample topography with Å resolution. This offers a unique method to directly relate electrical transport properties as given by the local ECP to the morphological features of the sample, such as grain boundaries, defects, and changes in composition. Moreover, STP provides a way to study electron transport phenomena beyond the macroscopic diffusive regime, e.g., by probing ballistic transport at small length scales and the wave nature of the charge carriers and the specifics of the Fermi surface. For instance, Friedel-like oscillatory terms emerge as a correction to the ECP in the vicinity of a point-like defect.[12,13] Theoretical predictions for impurities inside metals suggest that the magnitude of these oscillations is <1 μV for standard experimental current densities,[13] which is beyond experimental reach so far.

STP was first proposed by Muralt and Pohl[5] and subsequently implemented in different ways. A common approach is based on a single-tip STM[6–8] and two contacts that are used to apply a bias current across the sample. Another recent approach is the use of a multi-tip STM[9–11] where a current is applied via two outer tips placed in firm contact with the sample. An advantage of the multi-tip setup is the possibility to achieve higher local current density, thereby increasing the signal-to-noise ratio (SNR) without inducing strong Joule heating of the sample. However, it is difficult to determine the current distribution and its homogeneity through the sample. Multiple tips alleviate the efforts to fabricate *ex situ* electrical contacts to the sample due to the flexible positioning of the contact electrodes, but the operation of a multiple-tip setup can be quite complex. On the other hand, fabricating electrical connections to samples can be challenging due to the need of minimizing the contact resistances and sample contamination in the *ex situ* handling of the samples. Here, we will present an implementation of STP using the single-tip approach. Owing to its simplicity, our scheme provides a viable addition to most existing STM setups.

Different noise performances are reported for a variety of STP schemes, some claiming to be limited only by the Johnson–Nyquist thermal noise of the tunneling junction and others attributing a significant role also to the tunneling current amplifier. Both dc and ac schemes have been used to measure the ECP; however, it is not clear if one is superior to the other. Here, we present a complete noise analysis of a general STP implementation using either a dc or an ac detection scheme to identify the different noise contributions. We analyze both sample-and-hold and dual-feedback approaches and compare their advantages and disadvantages. Additionally, we discuss the role of the feedback control loop in the noise performance, which was previously not considered. Finally, we implement both dc and ac sample-and-hold measurement procedures into our setup and directly compare their performances using a resistor circuit and a current-biased epitaxial graphene sample. The measurements on the graphene highlight the importance of thermal effects in STP, which represent an additional source of noise and error that requires attention. Understanding of all the above-mentioned factors is necessary in order to achieve sub-μV resolution STP measurements. A high sensitivity will allow us to investigate the subtle modifications in the ECP due to the coherent wave nature of charge carriers at defects and charge and spin accumulations due to momentum and spin dependent scattering phenomena.[12,14]

II. STP METHOD

STP measures the ECP $\mu_{ECP}(x) = \mu_C(x) - e\phi(x)$, where $\mu_C(x)$ is the chemical potential and $\phi(x)$ is the electrostatic potential at tip position x. Experimentally, the ECP is measured in two main ways: the so-called sample-and-hold approach inherited from scanning tunneling spectroscopy (STS) and a dual-feedback approach. In the sample-and-hold approach, the z piezo-feedback signal controlling the tip–sample separation is turned off, effectively freezing the tip–sample separation at the setpoint value. Subsequently, the ECP voltage is measured, after which the z-feedback is restored to return to normal STM topography scanning. In this approach, the ECP can be measured in two ways. The first one is by performing a standard STS measurement[15] by acquiring an $I_t(V)$ curve, where I_t is the tunneling current and V is the sample bias voltage, while a bias current I_s is flowing through the sample [Fig. 1(a)] and determining the voltage $V = \mu_{ECP}$ for which $I_t = 0$, i.e., the value of the ECP. The second approach uses a feedback controller[5–11] to apply a compensation voltage V_c to either the sample or the tip to zero I_t, thereby equating

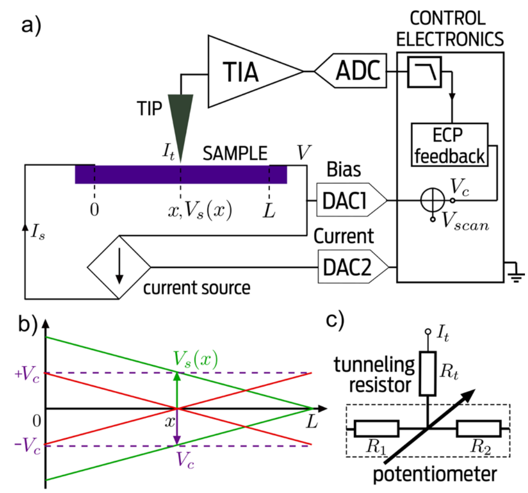

FIG. 1. (a) A simple schematic of the measurement setup. The sample bias current I_s is applied via a floating voltage-controlled current source (controlled by DAC2). I_s creates a voltage drop $V_s(x)$ across the sample at the position x of the tip. The bias voltage V is provided by DAC1, which can be used both for applying an STM scanning voltage (V_{scan}) or to compensate the surface ECP (V_c). Both DAC1 and DAC2 can also apply ac voltages and a superposition of ac and dc voltages, allowing for operation in both dc and ac modes. I_t is amplified by using the transimpedance amplifier (TIA) with a gain of 10^9 V/A and subsequently sampled by using the ADC. The ECP-feedback controls V_c in order to zero I_t. (b) I_s creates a voltage drop V_s across the sample, which is represented schematically for opposite current directions as the green lines. During the ECP measurement, $V_{scan} = 0$ and V_c is applied to the sample (dashed lines), fixing the potential on the right-hand side with respect to the reference potential of the tip. If $V_c = -V_s(x)$, then $I_t = 0$. The voltage $V_s + V_c$ is shown by the red lines. (c) The tip and sample in (a) can be schematically represented as a potentiometer and a tunneling resistor R_t. The sample resistance R_s is represented by using the potentiometer dividing R_s into two parts, from one side to the tip (R_1) and from the tip to the other side (R_2). Changing the tip position x changes R_1 and R_2, while $R_s = R_1 + R_2$ remains constant. Different values of R_t can be used to simulate different tip–sample distances.

the sample voltage $V_s = \mu_{ECP}$ and $-V_c$ [Fig. 1(b)]. This is a simplified description of the STP measurement. For details, see Sec. IV. V serves both for providing the STM scanning voltage denoted as V_{scan} and for zeroing I_t during the ECP measurement when V_{scan} is set to zero, i.e., $V = V_{scan} + V_c$. In the dual-feedback mode, V_{scan} and the ECP are separated, e.g., one is a dc (0 Hz) and the other is an ac (say 0.3–3 kHz) signal, allowing for the z-feedback and ECP-feedback to run simultaneously. In addition, an operational mode with both feedback controlling ac signals at different frequencies is conceivable.

Another STP implementation is based on scanning noise microscopy, where instead of I_t the junction thermal noise is used as the z-feedback input to stabilize the tip–sample separation.[16] Scanning noise potentiometry is implemented in the dual-feedback method, i.e., a dc feedback controlling the tip–sample separation by using the Johnson–Nyquist noise as an input and an ac feedback to compensate the ac tunneling current.[17] The method was reported having issues with artifacts and the noise not precisely following the expected Johnson–Nyquist behavior and, hence, was ultimately not further pursued. All the most recent STP implementations are feedback-based and use I_t for tip–sample separation stabilization. STP can also be implemented using atomic force microscopy (AFM), which allows for performing STP on micrometer- and nanometer-scale devices.[18,19] The AFM is operated in the oscillating mode with a low mechanical oscillation amplitude, and the force-feedback is used to maintain the tip–sample separation. A conductive AFM tip is used to measure I_t, and both dc and ac modes can be used to detect the ECP. AFM operation has a distinct advantage in enabling measurement of devices that are situated on non-conducting substrates.

Common to all STP measurements is a sample with resistance R_s with I_s flowing through it and a tip electrode having a high tunneling resistance R_t to a point on the sample, where I_t is measured with a transimpedance amplifier (TIA). We show in Fig. 1(a) our particular implementation where we use a floating voltage-controlled current source to apply I_s. The current source is controlled by the voltage output DAC2, whereas DAC1 is used to apply a potential V_c with respect to the tip reference (ground) to control I_t. I_s can also be applied directly via two independent voltage sources connected to each end of the sample. Let us quickly illustrate the simplest case of an STP measurement where all the voltages are dc. I_s results in a voltage drop across the sample length L. Directly under the tip, at position x, the local potential equals $V_s(x)$. For the two opposite directions of I_s, V_s is shown schematically with the green lines in Fig. 1(b). The potential on the right-hand side is determined by V_c. The voltage V_c (purple lines) can be used to zero I_t at position x (red lines), i.e., having the same potential as the reference. Note that a direct voltage measurement through the tip electrode is impeded by the large tunneling resistor. The picture presented in Fig. 1(b) is also valid for an ac STP measurement where now the lines (green, purple, and red) represent the envelopes of their respective ac voltages. If the phases of the two voltages $V_s(x)$ and V_c are aligned such that they are in-phase at position x as shown with the green and purple arrows, respectively, in Fig. 1(b), the ac component of I_t can be compensated to zero. The tip–sample junction can be modeled in a simple way by using a potentiometer and a tunneling resistor R_t, as shown in Fig. 1(c).

III. NOISE ANALYSIS

A. General considerations

For STP, the signal-to-noise ratio (SNR) can be defined as the ratio of the spatial slope of the ECP (in μV/nm) and the average noise in ECP (in μV). Note that the SNR of the ECP, would be the ECP itself over its root-mean-square (rms) noise value. The slope of the ECP is determined by the product of the sheet resistance and the current density. This renders the signal material-dependent and also hints that the signal cannot be increased indefinitely due to practical limitations on the bias current. Importantly, large excitation currents will lead to thermal drifts and an increased magnitude of the thermal voltage, thus imposing further constraints on measuring precisely the ECP. Furthermore, one may also be interested in different signals, e.g., the step resistance at boundaries or the magnitude of the aforementioned oscillations of the ECP. Hence, we will discuss in the following directly the rms noise as the quantity to be optimized since the total noise level will determine which phenomena can be investigated.

To understand the fundamental noise limitation of STP and to achieve the highest possible performance for an implementation of this technique, we first carry out a detailed noise analysis. The noise analysis is valid for all STP implementations because it is based on common basic assumptions. We proceed with a general examination of the tunneling current[20] and its noise contributions since the tunneling current is the main quantity of interest for the measurement of the ECP. We use the analysis to compare the different STP implementations.

The tunneling current depends on the current-to-voltage $I_t(V) = G(V)V$ characteristic of the junction (Fig. 2), where G is the local tunneling conductance, which generally depends on the tip–sample distance and applied voltage. For a slowly varying $I_t(V)$ characteristic, the tunneling current in the vicinity of a voltage V_{dc} can be written as

$$I_t(V_{dc} + \Delta V) \approx G(V_{dc})V_{dc} + g(V_{dc})\Delta V = I_{dc} + \Delta I_t. \quad (1)$$

The differential conductance $g(V) = dI_t/dV$ defines the change in I_t for a small additional ac voltage $\Delta V = V_{ac}\cos(2\pi f_0 t)$ superimposed on the dc voltage V_{dc} (Fig. 2). Furthermore, the tunneling conductance depends exponentially on the tip–sample distance z,

$$G(V_{dc}) = G_0(V_{dc})\exp[-\kappa z(t)], \quad (2)$$

where $\kappa = \sqrt{2m\Phi}/\hbar$ is the inverse decay length of the tunneling barrier and m is the mass of the electron. κ is often considered to be a constant defined by the average work function Φ of the tip and sample. Typically, κ amounts to 2 Å^{-1} and is assumed to be insensitive to a change in V_{dc} or z. Hence, all local electronic properties of the substrate are reflected in G_0. At an average tip–sample distance z_0, we thus have

$$I_{dc} = G_0(V_{dc})e^{-\kappa z_0}V_{dc}, \quad I_{ac} = g_0(V_{dc})e^{-\kappa z_0}V_{ac}. \quad (3)$$

The voltages V_{dc} and V_{ac} are time-dependent even when set to constant values due to the noise ν_v that arises from fluctuations in the surface potential due to noise in the current and voltage sources.

The tip–sample distance $z(t)$ can be expressed as a disturbance $z_n(t)$ added to the average distance z_0, i.e., $z(t) = z_0 + z_n(t)$. The peak-to-peak fluctuations of $z_n(t)$ are typically below several pm,

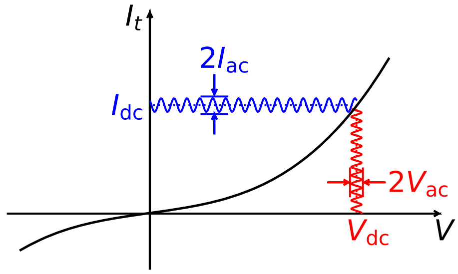

FIG. 2. A typical current-to-voltage $I_t(V)$ curve in an STM experiment where the conductance increases with the applied bias voltage. The applied sample bias V_{dc} sets the tunneling current I_{dc} in the junction. If we superimpose an ac voltage V_{ac} (red) onto the bias, the conversion rate to an ac current I_{ac} (blue) is given by the slope of the $I_t(V)$ curve. This slope $g(V) = dI_t/dV$ is referred to as the differential conductance. For small V_{ac}, it follows that $I_{ac} \approx g(V_{dc})V_{ac}$.

which is small compared to z_0. Thus, $\kappa z_n \ll 1$ and to first order in the expansion of the exponential function, we can write

$$I_t(t) \approx [I_{dc} + I_{ac}\cos(2\pi f_0 t) + i_v(t)][1+\eta(t)] + i_j(t) + i_a(t), \quad (4)$$

where we introduced the dimensionless parameter $\eta(t) = -\kappa z_n(t)$ and $i_j(t)$, $i_a(t)$, and $i_v(t) = v_v/R_t$ are the noise contributions due to the tunnel junction, the transimpedance amplifier, and fluctuations of the surface potential, respectively. Note that we use lower-case letters for the noise variables to emphasize that their mean value is zero. The parameter η quantifies the modulation of the instantaneous tunneling current by fluctuations in the tip–sample distance. We can estimate the magnitude of $|\eta|$ from the apparent peak-to-peak noise Δz_{pp} in [pm] in the topography to be $|\eta| \approx 0.023 \cdot \Delta z_{pp}/2$. Even when assuming relatively large noise amplitudes of $\Delta z_{pp} = 20$ pm, we have $|\eta| \approx 0.23$.

In order to determine i_v, we introduce a simple model for the sample. R_s is split into two parts: from one side of the sample (0) to the tip position (x) with resistance R_1 and from the tip to the opposite side (L) with resistance R_2 such that $R_s = R_1 + R_2$ [Fig. 1(c)]. For simplicity, we assume that R_s is the full sample resistance; however, we should be aware that a non-negligible part of V_s drops at the contacts to the sample. The current source applies I_s through the sample, creating a potential $V_s(x) = I_s R_2$ at position x with respect to the right-hand side. In addition, the tip–sample voltage $V_{dc}(x) = V_c + V_s(x)$ [Fig. 1(b)] at the position of the tip. Both V_s and V_c will lead to potential fluctuations v_v in V_{dc}. The corresponding current noise is $i_v = v_v/R_t$, where we have taken $R_t = (G_0 e^{-\kappa z_0})^{-1}$ at the setpoint value. Additional potential noise on the surface can arise from fluctuations in the contact resistances. Generally, the potential fluctuations may be considered small but can become significant when achieving ultimate signal-to-noise ratios.

B. dc mode

1. Simple model

We proceed with the simplest implementation of STP based on dc currents and voltages with a sample-and-hold mode (see Sec. II). In this mode, the tunneling current is

$$I_t(t) = [I_{dc} + i_v(t)][1+\eta(t)] + i_j(t) + i_a(t). \quad (5)$$

The local ECP of the surface is determined by compensating the tunneling current to $I_{dc} = 0$. The residual noise is given by

$$i_t(t) = i_v(t) + i_j(t) + i_a(t) + i_v(t)\,\eta(t) + I_{\text{off}}\eta(t). \quad (6)$$

We have introduced the term I_{off} that describes a constant offset current being present in the junction despite the compensation procedure to null the tunneling current. This term can arise due to small offsets in the analog-to-digital converter (ADC) or the transimpedance amplifier corresponding typically to a current of less than 0.1 pA. We will comment on the contribution of I_{off} in detail later when we estimate the contributions of all the terms in Eq. (6). Furthermore, from the above estimation $\eta \lesssim 0.2$, we can disregard the term $i_v \cdot \eta$ in comparison to i_v. The remaining noise sources in Eq. (6) are all independent of each other, and thus, the total power spectral density (PSD) of the noise is given by (for details, see Appendix A)

$$S_t = S_v + S_j + S_a + I_{\text{off}}^2 S_\eta. \quad (7)$$

We first look at the last term $I_{\text{off}}^2 S_\eta$. Note that the tip–sample variations will be larger with the topographic feedback turned off during the STP mode, increasing particularly the low frequency oscillations where the dc drifts of the tip–sample distance affect the STP measurements (see further below). In the following, we analyze the contribution of the offset term assuming a relatively large $\eta \approx 0.2$. Before starting a measurement, we adjust all offsets to zero in order to minimize I_{off}. In the electronics, the offset in voltage can be adjusted to better than $V_{\text{off}} < 0.1$ mV, corresponding to $I_{\text{off}} \approx 0.1$ pA depending on the gain of the transimpedance amplifier. For $\eta = 0.2$, we estimate that $S_\eta = 1.5 \cdot 10^{-7}$ Hz^{-1} assuming white Gaussian noise and a bandwidth of 10 kHz. We thus estimate $I_{\text{off}}^2 S_\eta \le 1.5 \cdot 10^{-33}$ A^2/Hz ($I_{\text{off}}\sqrt{S_\eta} = 0.04\,\text{fA}/\sqrt{\text{Hz}}$), which is much smaller than the thermal junction noise discussed below. However, most of the tip–sample fluctuations are concentrated at low frequencies, and with offset currents in the range of 1 pA, this contribution can become significant. Removing the offset current minimizes this term, and we can neglect it henceforth.

To get an idea on the total expected noise and the relative weights of the individual terms, we estimate now the noise contributions of the different sources, i.e., the voltage source, the current source, the tunneling junction, and the transimpedance amplifier, respectively (see Fig. 1). Most often, the noise specifications are given as the square root of the average PSD, i.e., $\sqrt{S}$, and hence, we will discuss this quantity in the following. We start with S_v representing the fluctuations in the tunneling current i_v due to noise in the surface potential v_v underneath the tip, $i_v = v_v/R_t$. The surface potential fluctuations arise from the bias source v_c and the current source given as $i_s R_2$; hence, $i_v = (v_c + i_s R_2)/R_t$. Translated into the power spectral densities, we have

$$S_v = \frac{S_c + R_2^2 S_s}{R_t^2}, \quad (8)$$

where S_s and S_c are the noise PSD of the current and voltage sources, respectively. The voltage to control the current source has a ten times lower noise figure than V_c (due to its range being ±1 V instead of ±10 V); therefore, its influence is neglected in the following. When using two DAC outputs to drive the bias current and provide a voltage reference, the term S_s drops out, but the contribution of S_c doubles. For an estimation of the noise, we assume that the voltage source at the full output range of ±10 V has an output noise of about $\sqrt{S_c} = 50\ \text{nV}/\sqrt{\text{Hz}}$. The current source for a gain of 1 mA/V has an output noise of $\sqrt{S_s} = 400\ \text{pA}/\sqrt{\text{Hz}}$. R_2 is usually several hundred Ω, and we assume that $R_2 = 500\,\Omega$ for the estimation. Finally, assuming that $R_t = 100\,\text{M}\Omega$, we obtain $\sqrt{S_v} = 4\,\text{fA}/\sqrt{\text{Hz}}$. We note that fluctuations of R_2 are also a possible source of noise, e.g., from contact resistance changes, which can be included in the S_s and S_c terms but are hard to quantify. The influence of contact resistance fluctuations can be reduced by minimizing environmental effects, e.g., the experiment in ultra-high vacuum and stable temperature, and placing the tip close to the voltage reference electrode.

Furthermore, the transimpedance amplifier noise is about $\sqrt{S_a} = 8\,\text{fA}/\sqrt{\text{Hz}}$. We should note that the transimpedance amplifier noise also depends on the source capacitance and resistance.[20]

We now discuss S_j in Eq. (7). The dominant noise term in the tunneling junction is the Johnson–Nyquist noise, which is given by

$$S_j(f) \approx \frac{4k_B T}{R_t}, \tag{9}$$

where k_B is the Boltzmann constant, T is the temperature, and R_t is the setpoint tunneling resistance, which we take again at its mean tip–sample distance z_0. It is important to note that in most cases, the tunneling resistance at zero gap voltage will be different from the setpoint chosen for topography. Usually, R_t at the zero bias is higher than at a finite bias, which can be determined by acquiring an $I_t(V)$ curve (Fig. 2). To provide a number for the thermal junction noise, we chose $R_t = 100\,\mathrm{M\Omega}$ at $T = 300$ K, which yields $\sqrt{S_j} = 13\,\mathrm{fA}/\sqrt{\mathrm{Hz}}$. For a more detailed discussion on other noise terms in the tunneling junction, see Appendix B.

The tunneling current is sampled by using the analog-to-digital converter (ADC) (cf. Fig. 1). This process adds the input noise of the ADC to the tunneling current signal, which also has to be taken into account. To add the two noise sources, the tunneling current has to be converted into a voltage as given by the gain k of the transimpedance amplifier. The voltage value in the electronics representing the tunneling current corresponds to the surface ECP by a multiplication factor R_t/k. Assuming flat spectrum (Gaussian) noise sources, we can write for the rms noise of the ECP as seen in the tunneling current measurement,

$$\mu_{ECP}^{rms} = \frac{R_t}{k}\sqrt{k^2 \cdot S_t + S_{ADC}} \cdot \sqrt{BW}. \tag{10}$$

Note that we assume the overall bandwidth BW of the measurement to be smaller than the intrinsic bandwidths of the individual sources, i.e., in particular the bandwidth of the transimpedance amplifier. The ADC has a typical noise of $\sqrt{S_{ADC}} = 250\,\mathrm{nV}/\sqrt{\mathrm{Hz}}$ corresponding to an apparent current noise of $\sqrt{S_{ADC}}/k = 0.25\,\mathrm{fA}/\sqrt{\mathrm{Hz}}$. This term is negligible with respect to the other noise sources, but we keep it for completeness because of its dependence on the gain of the amplifier. This completes our estimation of the individual terms in Eq. (10), and we can finally write the total ECP rms noise as

$$\mu_{ECP}^{rms} = \frac{R_t}{k}\sqrt{k^2\left(\frac{S_c + R_2^2 S_s}{R_t^2} + \frac{4k_B T}{R_t} + S_a\right) + S_{ADC}} \cdot \sqrt{BW}$$
$$= \sqrt{S_c + R_2^2 S_s + 4k_B T R_t + R_t^2\, S_a + \frac{R_t^2}{k^2} S_{ADC}} \cdot \sqrt{BW}. \tag{11}$$

The ECP rms noise clearly depends on both R_t and T, as illustrated in Fig. 3. In general, R_t should be made as small as possible to obtain the lowest noise. However, very low R_t means very short tip–sample distances, which increases the risk of crashing the STM tip into the sample and makes the tunneling very unstable. For this reason, we only show the calculation down to $R_t = 10\,\mathrm{M\Omega}$ that can be realistically obtained. For $R_t > 300\,\mathrm{M\Omega}$, the amplifier noise is the main factor and the total noise is well described by the amplifier and junction contributions added together [cf. Fig. 3(a)]. However, for $R_t < 300\,\mathrm{M\Omega}$, the relative contribution of the junction noise exceeds the noise of the amplifier. For $R_t < 100\,\mathrm{M\Omega}$, the total noise is essentially given by the junction noise. In addition, at $R_t < 50\,\mathrm{M\Omega}$, the contribution from the surface potential noise becomes significant and eventually exceeds the amplifier noise. By lowering T, the junction noise can be significantly reduced [cf. Fig. 3(b)]. For $R_t = 100\,\mathrm{M\Omega}$ and $T < 50$ K, the amplifier noise exceeds again the junction noise. In the best conditions, i.e., low R_t and low T, the surface potential variations can become dominant, ultimately limiting the noise performance. Furthermore, it is interesting to note that the total noise will depend on k [Eq. (11)]. On the other hand, the noise and bandwidth of the amplifier go down with increasing k, giving some room for improvement. As will be discussed in Subsection IV B, we also need to consider the cabling for the tunneling current from the tip to the amplifier that can lead to quite different noise figures for S_a.[20]

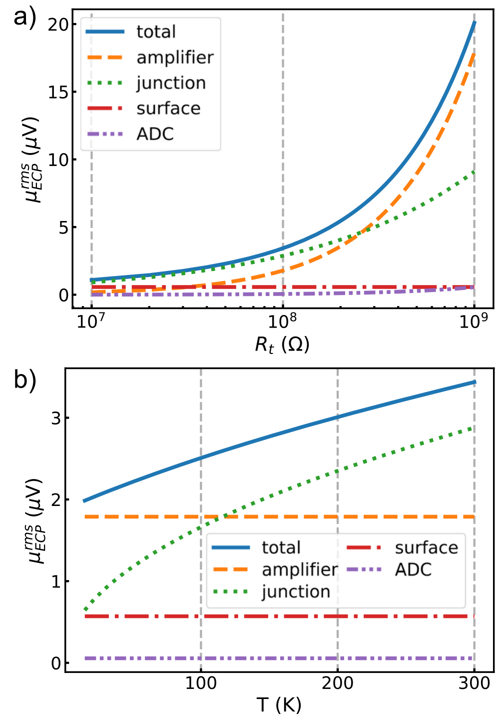

FIG. 3. Estimated individual noise contributions to the ECP according to Eq. (11). The total noise contains all contributions, i.e., the surface potential, the junction, the amplifier, and the ADC. The graphs show μ_{ECP}^{rms} (a) as a function of R_t at $T = 300$ K and (b) the dependence on temperature T for $R_t = 100\,\mathrm{M\Omega}$. The parameters used for the plots are $k = 10^9$ V/A, $BW = 5$ Hz, $\sqrt{S_{ADC}} = 250\,\mathrm{nV}/\sqrt{\mathrm{Hz}}$, $\sqrt{S_a} = 8\,\mathrm{fA}/\sqrt{\mathrm{Hz}}$, $\sqrt{S_s} = 400\,\mathrm{pA}/\sqrt{\mathrm{Hz}}$, $R_2 = 500\,\Omega$, and $\sqrt{S_c} = 50\,\mathrm{nV}/\sqrt{\mathrm{Hz}}$.

Our simple estimation clearly shows that the noise of the surface potential can play a major role in the total ECP noise alongside the junction and amplifier noise (Fig. 3). However, there are two ways to reduce the surface potential contribution. First, we can reduce the influence of the voltage source by voltage dividing its output. There is, however, a trade-off because the range of the output is also reduced and one may not be able to achieve compensation of I_t to zero anymore if the surface ECP value exceeds the range of the voltage source. Second, we can reduce the influence of S_s by reducing its prefactor R_2 [Eq. (11)]. A significant part of R_2 also stems from contact resistance. Therefore, it is best to measure as close as possible to the sample contact to DAC1 and reduce the contact resistance as much as possible. Experimentally, these might be challenging tasks and will strongly depend on how the sample contacts are made. Additionally, a measurement geometry with a fourth electrode providing a voltage reference close to the STM tip can be used to reduce the influence of R_2.

2. Influence of the PI controller

Until now, we have not considered the fact that STP is a compensation measurement and that the compensation voltage is controlled by a closed-loop feedback, for which we use a proportional-integral (PI) controller. Apart from that, we have also disregarded any non-Gaussian behavior in our noise sources, which is not realistic; see Appendix A. The PI controller in closed-loop operation outputs the compensation voltage V_c to zero I_t. In Appendix D, we calculate the closed-loop transfer function of the PI controller and show that the system is always stable when out of the oscillatory response regime. We also show that there is no finite steady-state error, i.e., the controller can precisely compensate I_t to zero.

After a settling time, the PI controller compensates I_t to zero and we sample and average the closed-loop controller output for a given time t_{avg} to obtain the ECP. Averaging for a time t_{avg} is equivalent to a moving average filter with a frequency response F_{avg}. Thus, we have an expression for the ECP rms noise

$$\mu_{ECP}^{rms} = \sqrt{\int_0^{+\infty} S_n(f)|H_{PI}(f)|^2|F_{avg}(f)|^2 \mathrm{d}f}, \qquad (12)$$

where

$$S_n = S_c + R_2^2 S_s + 4k_B T R_t + R_t^2 S_a + \frac{R_t^2}{k^2} S_{ADC} \qquad (13)$$

is the total noise PSD and H_{PI} is the closed-loop transfer function of the PI controller. Together, H_{PI} and F_{avg} define the overall bandwidth of the ECP measurement. It is important to note that the expression for S_n is valid exclusively when the cut-off frequency of the digital filter inside of the electronics is lower than the TIA cut-off frequency. See Appendix D for more details on how to derive S_n. Equation (12) simplifies to Eq. (11) when we assume a step function with a BW corresponding to $1/2t_{avg}$ instead of $|H_{PI}(f)|^2|F_{avg}(f)|^2$ and a flat spectrum for S_n.

An important question is what is the optimal setting to achieve a fast response and low noise in STP measurement at the same time. To this end, we consider two quantities of interest, the ECP rms noise μ_{ECP}^{rms} and the settling time of the feedback. The latter is the time it takes for the controller to achieve compensation of the tunneling current to within a given error. We use an error band that is equal to one percent of the step excitation and obtain the settling time directly from the step response (Appendix D). The settling time is effectively the minimum time we have to wait before we can start the data averaging, which directly influences the overall measurement time. Figure 4 shows the dependence of μ_{ECP}^{rms} and settling time on the integral gain K_i for (a) R_t = 100 MΩ and (b) R_t = 1 GΩ. The settling time has a clear minimum for a small range in K_i. On the other hand, μ_{ECP}^{rms} shows a peculiar behavior. It is nearly constant for a broader range in K_i but increases abruptly for large K_i and decreases also sharply for very low K_i. At high gains, the system becomes unstable and goes into oscillations. It may appear advantageous to work at low gains since the noise is considerably reduced. However, the settling time increases rapidly, indicating that the transfer function

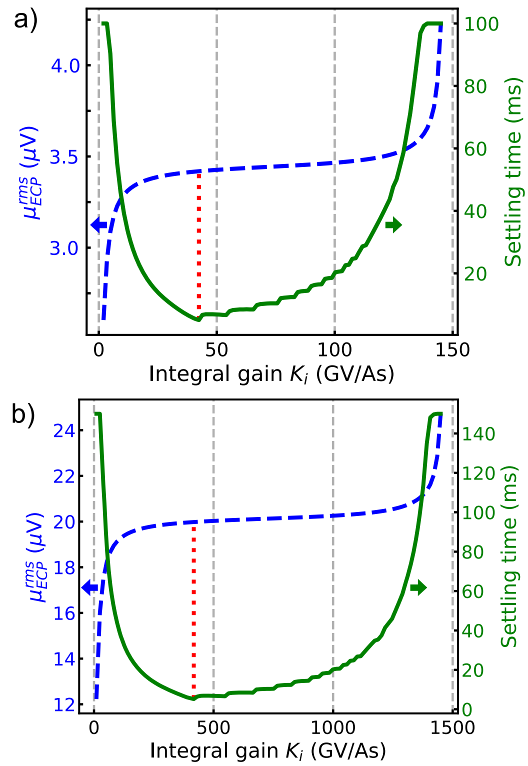

FIG. 4. ECP rms noise μ_{ECP}^{rms} and settling time dependence on the integral gain K_i for (a) R_t = 100 MΩ and (b) R_t = 1 GΩ. For both (a) and (b), we have used the same estimation for the noise terms as in the simple estimation in Fig. 3 and an averaging time t_{avg} = 100 ms. The minimum settling time to reach an accuracy of 1% in both (a) and (b) is marked with a vertical red dotted line.

of the PI controller dominates the bandwidth (Appendix D). The overall behavior appears very similar for R_t = 100 MΩ and 1 GΩ; however, a notable difference is that the ranges of K_i yielding short settling times and constant μ_{ECP}^{rms} differ by an order of magnitude. This is not unexpected since K_i and R_t appear together as a K_i/R_t term if we disregard K_p (Appendix D). This fact reveals a subtle inadequacy of the PI controller. If, for example, we measure two different neighboring regions on the surface that differ significantly in the local density of states and thus effectively in R_t at zero gap voltage in the STP mode, a single K_i value will not be optimal for measuring the ECP in the two areas. The compensation will not be optimal either in terms of noise or in cases where the two regions differ in R_t by more than an order of magnitude, not compensate at all for one of the regions. If we recall the definition of R_t as the slope of the $I_t(V)$ curve at $V = 0$, we can envision these regions as one having a conductive curve and the other having a semi-conductive $I_t(V)$ curve. This can become relevant for measuring ECP across grain boundaries in thin films since locally in such heterogeneous samples, the local $I_t(V)$ characteristic might vary a lot. This could be overcome by tracking the local $I_t(V)$ characteristics and adapting K_i accordingly by an automatic routine. This hints at the possibility for better controllers, which could dynamically adjust the gain factors in order to achieve the optimal signal-to-noise ratio.

In the analysis above, we assumed flat noise spectral densities. Hence, narrowing the bandwidth will reduce the passing noise to near zero frequency. However, in nearly all electronics and physical systems, the noise is not flat in the frequency domain but rather increases quickly toward lower frequencies, i.e., flicker noise. Hence, a further reduction in the bandwidth will not increase the signal-to-noise ratio efficiently beyond a certain point. To determine the effect of flicker noise on μ_{ECP}^{rms}, we estimate its contribution in our STP measurement setup. The flicker noise is usually of the form

$$S_{flicker} = \frac{B}{(f/\mathrm{Hz})^{\gamma}}, \tag{14}$$

where B is a constant in units of V^2/Hz and $\gamma \approx 1$. Let us assume that $\gamma = 1$, $B_{ADC} = 10 \cdot 10^{-12}\ \mathrm{V}^2/\mathrm{Hz}$, and $B_{DAC} = 2 \cdot 10^{-12}\ \mathrm{V}^2/\mathrm{Hz}$. The presence of flicker noise in the ADC and DAC noise leads to a significant increase in their contributions to the total ECP rms noise (Fig. 5). The ADC noise contributes more significantly for larger R_t, and the DAC noise (included in the surface potential noise) is independent of R_t, as shown in Eq. (11). The comparison between Figs. 3(a) and 5 highlights the significant role of the flicker noise in the dc mode.

C. ac mode

The flicker noise contribution severely limits the achievable performance for the dc mode of the ECP measurements (Fig. 5). The general strategy to circumvent the low frequency noise is to use ac excitation schemes and a lock-in detection, essentially shifting the bandwidth of the system around some center frequency f_0. Such a strategy can also be followed for the ECP measurements and will be denoted as the ac mode.

The local potential V_{ac} under the tip is composed of two ac voltages due to the ac bias current on the one hand, μ_{ECP}, and the ac compensation voltage V_c on the other hand. It is worth to carry out the analysis assuming a phase mismatch φ between these two voltages,

$$V_{ac}\cos(2\pi f_0 t + \delta) = \mu_{ECP}\cos(2\pi f_0 t) + V_c\cos(2\pi f_0 t + \varphi). \tag{15}$$

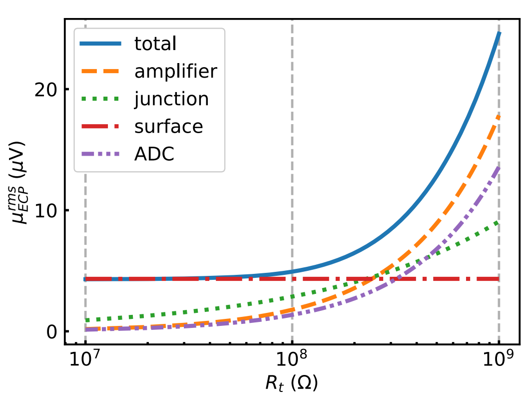

FIG. 5. μ_{ECP}^{rms} dependence on R_t with the flicker noise contributions of the ADC and DAC included. For the ADC and DAC flicker noise, we have used $B_{ADC} = 10 \cdot 10^{-12}\ \mathrm{V}^2/\mathrm{Hz}$, $\gamma_{ADC} = 1$ and $B_{DAC} = 1 \cdot 10^{-12}\ \mathrm{V}^2/\mathrm{Hz}$, $\gamma_{DAC} = 1$, respectively. The remaining Gaussian noise contributions and BW are the same as in Fig. 3 (T = 300 K).

One finds that

$$\begin{aligned} V_{ac} &= \pm\sqrt{\mu_{ECP}^2 + V_c^2 + 2\mu_{ECP}V_c\cos\varphi}, \\ \tan\delta &= \frac{V_c\sin\varphi}{\mu_{ECP} + V_c\cos\varphi}, \end{aligned} \tag{16}$$

where $\delta \in [-\pi/2, +\pi/2]$ [Figs. 6(a)–6(c)]. In the ac mode, the tunneling current [Eq. (4)] is demodulated with a lock-in by multiplying the input with $\cos(2\pi f_0 t)$ and $\sin(2\pi f_0 t)$ followed by a low-pass filter to extract the in-phase $I_{\mathrm{ac,X}}$ and out-of-phase $I_{\mathrm{ac,Y}}$ components, respectively [Fig. 6(d)]. The total measured signal is $I_{\mathrm{ac,meas}} = \sqrt{I_{\mathrm{ac,X}}^2 + I_{\mathrm{ac,Y}}^2}$. This means that we set the lock-in phase to be equal to the ECP phase, which, in this case, is zero [see Eq. (15)]. This is done by maximizing $I_{\mathrm{ac,X}}$ when $V_c = 0$. When $V_c \neq 0$, the lock-in phase would be set to δ instead of the phase of the ECP signal.

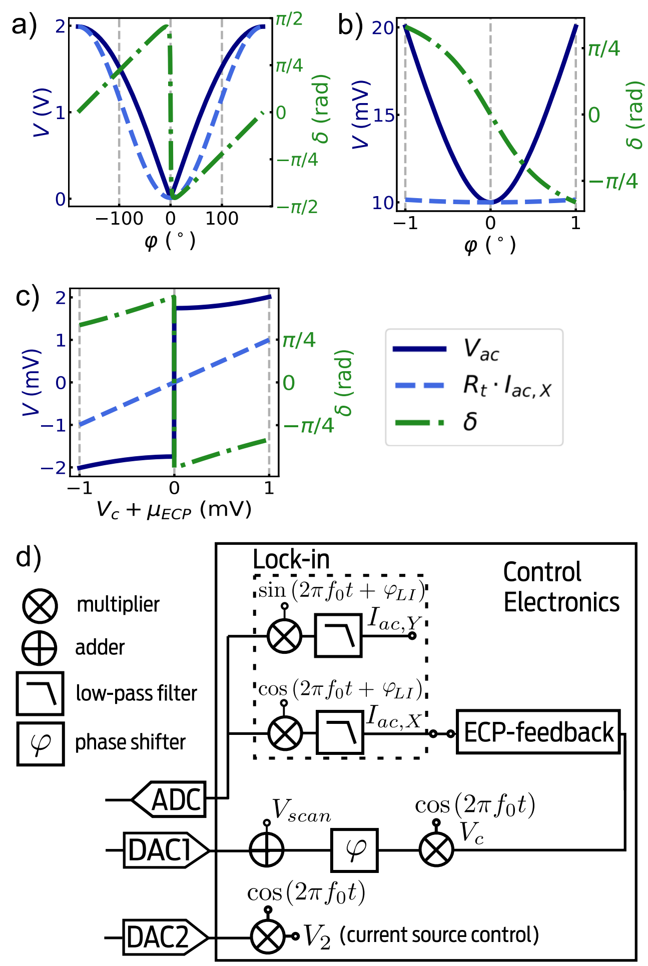

FIG. 6. (a) Dependence of V_{ac}, δ [from Eq. (16)], and $I_{ac,X}$ on the relative phase between the ECP and the compensation voltage φ. (b) Details of (a) around 0°. We used $\mu_{ECP} = 1$ V and $V_c = -0.99\mu_{ECP}$. (c) The total voltage, phase, and lock-in in-phase component dependence on the difference between the ECP and compensation voltage. We used $\varphi = 0.1°$. (d) Schematic representation of the lock-in amplifier that is integrated into the control electronics and used for the ac mode STP measurement.

We can see from Eq. (16) that the resulting voltage V_{ac} will only vanish if besides $\mu_{ECP} = -V_c$ the condition $\cos\varphi = 1$ is also fulfilled. If we assume that the amplitude of V_c has opposite sign to μ_{ECP}, the resulting voltage is minimized for $\varphi = 0$. Thus, we can determine φ by finding the minimum in $I_{\mathrm{ac,X}}$ when sweeping φ. If φ is not perfectly adjusted, the ac tunnel current cannot be fully zeroed but will always remain finite, i.e., $I_{ac} \neq 0$. The phase matching problem can be made simpler by using two DAC outputs with the same phase to drive an ac voltage across the device. In this case, the feedback only acts on the amplitudes of the two ac voltage sources and a vanishing ac tunneling current can be achieved. $I_{\mathrm{ac,X}}$ remains linearly dependent on the compensation voltage even when the phase between ECP and compensation voltage is not perfectly adjusted [Fig. 6(c)], making it a reliable input for the controller.

A detailed analysis of the noise in the ac tunneling current is given in Appendix E. The total PSD of the ac mode for positive frequencies is

$$\begin{aligned} S_{t,ac} &= I_{ac}^2 S_\eta(f) + S_v(f-f_0) + S_j(f-f_0) + S_a(f-f_0) \\ &\quad + I_{dc}^2[S_\eta(f-f_0) + 2\delta(f-f_0)] \\ &\quad + \frac{1}{4} I_{ac}^2 [S_\eta(f-2f_0) + 2\delta(f-2f_0)]. \end{aligned} \tag{17}$$

The shifted PSD functions indicate that the filter transfer function has to be shifted to the center frequency f_0 or $2f_0$ (cf. Appendix E). In comparison with the noise PSD of the dc mode [Eq. (7)], we notice that S_η also contributes with its low frequency components and that any finite ac current (I_{ac}) takes the role of I_{off} in the dc mode. The noise contributions of S_v, S_j, and S_a are the same as for the dc mode but need to be integrated with a shifted filter transfer function at the center frequency f_0. Note that the integration with the shifted filter transfer function essentially doubles the bandwidth, as it is performed symmetrically around the center frequency f_0. Thus, for a flat PSD, the noise contributions are doubled with respect to the dc mode. However, a gain in noise performance is achieved by moving away from $1/f$ noise, which can easily be a factor larger than 2 compared to the baseline noise at higher frequencies. In the ac mode, we also find additional noise terms proportional to I_{dc}^2 and I_{ac}^2 near the frequencies f_0 and $2f_0$, respectively. Both depend on the PSD of the tunnel junction noise and the filter transfer function at these frequencies.

It is important to achieve $\varphi = 0$ to allow for the feedback to zero I_{ac} completely; otherwise, one has

$$I_{ac} = \frac{|\mu_{ECP}\sin\varphi|}{R_t} \approx \frac{|\mu_{ECP}\,\varphi|}{R_t}. \tag{18}$$

As an example, by taking $\varphi = 0.1^\circ$ and $|\mu_{ECP}| = 1$ V, we get $V_{ac} = \mu_{ECP}\sqrt{1-\cos^2\varphi}$, which amounts to about 1.7 mV [Fig. 6(c)], resulting in a systematic error in measuring μ_{ECP} of 1.5 μV. The noise contribution proportional to I_{dc} is more difficult to avoid since I_{dc} originates from a constant thermal voltage on the order of a few mV between the sample and the tip due to finite differences in their temperatures. We discuss this in more detail in Sec. IV. A properly chosen low-pass filter with effective cut-off frequency lower than $f_0/2$ will be very efficient in removing the contributions $I_{dc}^2\delta(f-f_0)$ and $I_{ac}^2\delta(f-2f_0)$ as long as I_{dc} and I_{ac} are not very large, which we ensure by setting the dc gap voltage to zero and by setting φ properly. Hence, we can disregard these two terms.

We can make a simple estimation for the total rms noise of the ECP in the ac measurement mode in a similar way as we have done for the dc case. First, we write the final expression for the rms ECP noise

$$\begin{aligned} \mu_{ECP}^{rms} &= \left[k^2\left(\frac{I_{ac}^2}{2}S_\eta + \frac{S_c + R_2^2 S_s}{R_t^2} + \frac{4k_BT}{R_t} + S_a\right) + S_{ADC}\right]^{1/2} \cdot \frac{R_t}{k}\sqrt{2\,BW} \\ &= \left[\frac{1}{2}I_{ac}^2R_t^2S_\eta + S_c + R_2^2S_s + 4k_BTR_t + S_aR_t^2 + \frac{R_t^2}{k^2}S_{ADC}\right]^{1/2} \cdot \sqrt{2\,BW}. \end{aligned} \tag{19}$$

The factor $\sqrt{2}$ is due to the doubled bandwidth discussed above. We again assume all noise sources to be Gaussian, i.e., the spectral densities are independent of the frequency. In the ac case, this is a much better approximation than in the dc case as we specifically choose f_0 with a flat noise spectrum within the bandwidth of the lock-in filter. We already estimated that $S_\eta \approx 1.5 \cdot 10^{-7}$ Hz^{-1} previously. For S_j and S_v, we use Eqs. (8) and (9), respectively, and $\sqrt{S_a} = 8\,\mathrm{fA}/\sqrt{\mathrm{Hz}}$.

In Fig. 7, we see that the ECP rms noise strongly depends on R_t and T, similarly as in the dc case (Fig. 3). However, there is a marked difference between the ac and dc cases. For the same averaging time as in the dc case, the ac mode has a factor $\sqrt{2}$ higher rms noise if we do not consider $1/f$ noise in the dc mode. Besides S_j, S_a and S_v, which we have already identified in the dc mode as important noise sources, we have an additional term proportional to I_{ac} in the ac mode. I_{ac} can be minimized by ensuring a good phase match between the ECP and compensation voltages. The term proportional to I_{ac} scales linearly with φ and becomes significant for $\varphi > 0.1^\circ$.

It is important to discuss the role of the low-pass filter in the ac mode especially in relation to the PI controller and how it affects the overall closed-loop behavior of the system. We can draw a parallel between the dc and the ac mode closed-loop behavior by noting that the only difference is the demodulation in the ac mode, which shifts the frequency spectrum by f_0 such that the signal of interest is shifted to 0 Hz. Thereafter, the low-pass filter removes the multiples of f_0 and creates a dc input signal for the PI controller. Therefore, the behavior of the closed-loop feedback in the ac mode is analogous to the behavior in the dc mode. We should emphasize that it is still important to choose the low-pass filter cut-off frequency appropriately, namely, such that it removes any multiples of f_0 while simultaneously keeping a sufficiently large bandwidth to allow the feedback to react promptly.

D. Dual-feedback operation

Even though our experimental STP implementation in both the dc and ac cases is a sample-and-hold implementation, we can still comment on the dual-feedback implementations based on our noise analysis. An advantage of the dual-feedback mode is the better tip stability, which allows for longer acquisition times without the fear of a tip crash due to drift in the z direction. On the other hand, drifts in the x and y directions cannot be mitigated by an additional feedback, which can reduce the lateral resolution of an ECP map. An active z-feedback can be an advantage when measuring with low

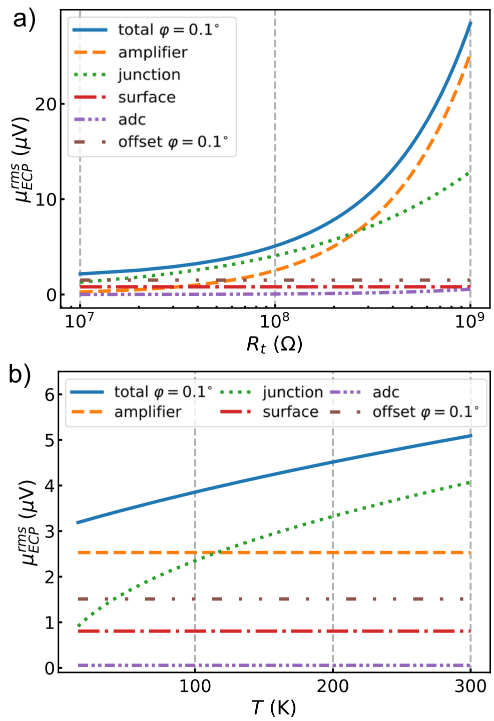

FIG. 7. Estimation of the ECP noise for the ac mode. The total noise contains all contributions, i.e., the surface potential, the junction, the amplifier, and the input noise of the ADC [cf. Eq. (19)]. The influence of a phase mismatch of $\varphi = 0.1°$ is also shown. The parameters used for the plots are $k = 10^9$ V/A, $BW = 5$ Hz, $\sqrt{S_{ADC}} = 250$ nV/$\sqrt{\text{Hz}}$, $\sqrt{S_a} = 8$ fA/$\sqrt{\text{Hz}}$, $\sqrt{S_s} = 400$ pA/$\sqrt{\text{Hz}} \cdot R_2$, and $\sqrt{S_{DAC1}} = 50$ nV/$\sqrt{\text{Hz}}$. (a) μ_{ECP}^{rms} dependence on R_t at $T = 300$ K. (b) μ_{ECP}^{rms} dependence on T at $R_t = 100$ MΩ.

tunneling resistances, i.e., when being close with the tip to the surface. Furthermore, in the dual-feedback implementations, there are additional effects and noise contributions, which are absent in the sample-and-hold implementation on which we comment individually for each case below. Additionally, the dual-feedback operation is more complicated to implement and requires both more electronic components and more complex programming.

In the dual-feedback mode, an ac tunneling current is used to control the z-feedback and the dc tunneling current is zeroed with the ECP-feedback. If $I_t(V)$ is non-linear, the ac signal can be rectified into a dc contribution via the second derivative of $I_t(V)$. To show this, we apply a Taylor expansion to I_t up to second order and define $\Delta V = V_{ac}\cos(2\pi f_0 t)$,

$$I_t = I_{dc} + g(V_{dc}) \cdot V_{ac}\cos(2\pi f_0 t) + \left.\frac{d^2 I}{dV^2}\right|_{V_{dc}} \cdot \frac{V_{ac}^2}{2}\cos^2(2\pi f_0 t) + \cdots. \tag{20}$$

By making use of $\cos^2(x) = (1 + \cos 2x)/2$, we can see that the second-order rectification term in Eq. (20) is given by

$$\Delta I = \frac{V_{ac}^2}{4}[1 + \cos(4\pi f_0 t)] \left.\frac{d^2 I}{dV^2}\right|_{V_{dc}}, \tag{21}$$

which contains a constant term proportional to V_{ac}^2. This directly shows that for a dual-feedback STP implementation where dc is used to measure the ECP and ac to control the tip–sample separation, there would be an intermixing of the ac signal into the ECP channel for a non-linear characteristic of the junction $I_t(V)$. This has to be taken into account for such implementations.

On the other hand, if we use a dc tunneling current to control the z-feedback and measure the ECP with an ac signal, the noise term proportional to I_{dc} in Eq. (17) becomes large and difficult to remove with a low-pass filter. Additionally, a shot noise term proportional to I_{dc} appears as well (see Appendix B). Therefore, a dc z-feedback with an ac ECP-feedback implementation is not optimal.

IV. EXPERIMENTAL IMPLEMENTATION

We present here a straightforward implementation of STP in a commercial ultra-high vacuum STM (RHK Pan-Scan), which can be easily adapted to any STM setup. The only addition to our STM electronics (RHK R9) is a commercial (SRS CS580) voltage-controlled current source used to bias the sample that is operated in the floating mode. Next to the STM chamber (housing the microscope head), an additional ultra-high vacuum chamber (base pressure $1 \cdot 10^{-10}$ mbar) serves for *in situ* sample preparations through various sputtering, annealing, and deposition techniques. There are five electrical contacts leading to the sample inside the STM head that allow us to perform four-point electrical transport measurements simultaneously with the STM measurements.

Two sample contacts inside the STM can be used to pass a current through a conductive sample via the voltage-controlled current source. The digital-to-analog output DAC2 (range ±1 V) from the R9 electronics is used to control the current (Fig. 1). The output DAC1 (range ±10 V) of the R9 electronics is used for applying a bias voltage and the ECP compensation voltage to the sample. The tunneling current is measured between the scanning tip and the sample using a transimpedance amplifier (RHK IVP-300, with 10^9 V/A gain) and sampled with an analog-to-digital (ADC) input. Both DACs and the ADC have a 16-bit resolution and are operated at a 1 MHz sampling rate. The R9 control software allows for controlling the output of different ac and dc channels. The signals are all added digitally inside the electronics and finally only output by the DACs, which allows for our STP implementation to be fully controlled by software. However, the two DAC outputs cannot be configured to directly drive the bias current and apply the compensation and gap voltages.

A. dc mode

In the dc mode, the tunneling current signal is first low-pass filtered before entering the PI feedback controller for ECP control. The setpoint of the ECP-feedback controller is set to zero, and its output is added to the bias voltage. In the STP measurement mode, we perform the topography scans, while the current is flowing through the sample. In a current-biased sample, the $I_t(V)$ curve is offset horizontally by the local sample voltage, $V_s^{\pm}$, where ± denotes the current direction (Fig. 8). To achieve the same gap voltage with $I_s \neq 0$ as with $I_s = 0$, we offset the bias voltage $V = V_{scan} + V_s^{\pm}$, with the scanning voltage V_{scan}. Throughout the entire measurement, the

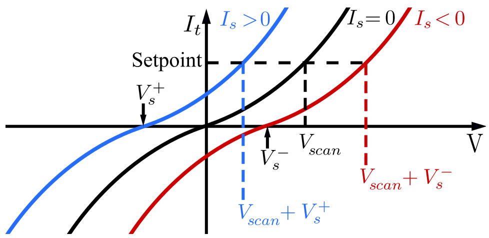

FIG. 8. Schematic showing the $I_t(V)$ curve profiles for zero bias current (black), positive bias current (blue), and negative bias current (red). Without a bias current, the scanning parameters are defined by the scanning voltage V_{scan} between the tip and the sample and the tunneling current setpoint. When a current flows through the sample, the $I_t(V)$ curve for zero current (black) is shifted horizontally by a value $V_s^{\pm}$ depending on the current direction. The appropriate applied bias to achieve the same gap voltage and current setpoint is then $V_{scan} + V_s^{\pm}$.

bias current is never turned off because changing I_s creates heating and cooling cycles that cause thermal expansion and contraction of the sample, which is detrimental for the stability of the tunneling junction. Hence, the thermal stabilization of the system is crucial for the measurements. To minimize these problems, we perform sub-millisecond current polarity switches, thereby creating only very short periods in which the bias current is not flowing through the sample. During current polarity switching, we simultaneously sweep I_s and V, thereby keeping I_t constant.

A block diagram of the acquisition of one data point in the dc mode is shown in Fig. 9. First, a current $I_s > 0$ is applied to the sample and the bias is set to $V = V_{scan} + V_c^+$. As soon as the tip–sample separation is stable (sample well thermalized), we freeze the z-feedback. V is set to a fixed value V_c^+ that is within a mV from the actual sample voltage V_s^+. Then, the ECP-Feedback is engaged to compensate the tunneling current fully to zero. We usually wait for 5–10 ms for the feedback to settle and then start the acquisition of the ECP-feedback signal with $t_{avg} = 50$–300 ms. We denote the acquired result $V_+ = V_c^+ + \Delta V_c$, where ΔV_c is the feedback-controlled voltage that compensates the current precisely to zero, i.e., V_+ precisely compensates V_s^+. The ECP-feedback is then frozen, and we simultaneously reverse the current direction and set $V = V_{scan} + V_c^-$. The z-feedback is activated, and we wait for it to stabilize the tip–sample separation around 10–50 ms. Thereafter, we disable the z-feedback and ramp V to V_c^- to acquire the ECP-feedback signal. The acquired value is $V_- = V_c^- + \Delta V_c$. After that, we switch the current direction again. We set $V = V_{scan} + V_c^+$ and acquire the topography, thus completing the data acquisition for one point. The tip now moves on to the next point. In order to avoid large tunneling current pulses in the case of a sudden overreaction of the feedback to a transient, we keep the compensation voltage limited to within a few mV. This ensures a stable tunneling junction throughout the entire measurement procedure.

The Joule heating increases the sample temperature relative to the tip temperature up to a few K depending on the applied current and the cooling power of the flow cryostat. The temperature difference generates a thermoelectric voltage between the tip and the sample. In the Tersoff–Hamann model of an STM junction, the thermal voltage is given as[21]

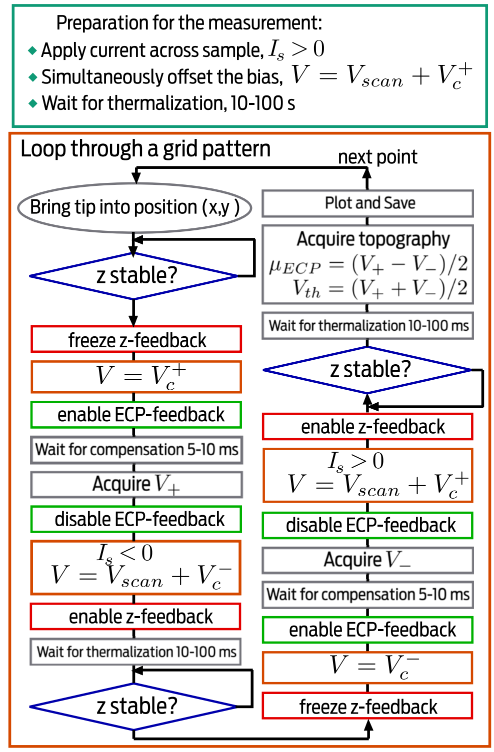

FIG. 9. A block diagram of a single point acquisition in the dc mode ECP measurement.

$$V_{th} = \frac{\pi^2 k_B^2}{6e}\left(T_T^2 - T_S^2\right)\left(\frac{1}{\rho_T}\frac{\partial \rho_T}{\partial E}\bigg|_{E_F} + \frac{1}{\rho_S}\frac{\partial \rho_S}{\partial E}\bigg|_{E_F, z=0} + \frac{z}{\hbar}\sqrt{\frac{2m}{\Phi}}\right), \tag{22}$$

where T_T and T_S are the temperatures and ρ_T and ρ_S are the local density of states of the tip and sample, respectively. In the dc mode, both V_{th} and μ_{ECP} contribute to I_t. We perform current polarity switching measurements in order to distinguish μ_{ECP} (dependent on current direction) from V_{th} (independent of current direction). We calculate the two from our measured compensation voltages V_+ for positive and V_- for negative current direction,

$$\mu_{ECP} = \frac{1}{2}(V_+ - V_-) \tag{23}$$

and

$$V_{th} = \frac{1}{2}(V_+ + V_-). \tag{24}$$

It is important to consider the influence of long term drifts in the electronics (e.g., voltage drifts dependent on slow lab temperature changes) on the measurement of the ECP and the thermal voltage. Because of the extraction procedure in Eqs. (23) and (24), it follows that any long term drifts in the compensation voltage will be eliminated from the ECP signal; however, they will remain present in the thermal voltage. To remove the long term drifts in V_{th}, we perform a line-by-line mean value subtraction for each image acquired. This is justified since we are only interested in the relative changes in V_{th}. The acquisition of a single scan line takes usually on the order of one to a few minutes for which the electronics drift is negligible. Furthermore, V_{th} depends on the logarithmic derivative of the local density of the tip, which may change while scanning over the substrate, whereas the ECP should not depend on the tip states. However, the tip states can influence the noise in the ECP significantly. For instance, with a tip with a semi-conducting character R_t at zero bias voltage becomes large and the noise in the ECP increases.

The single point current reversal method described above makes our dc mode measurement quite robust against drifts, both in the x and y directions in scanning and long term drifts in the compensation voltage. Other dc methods that have previously been implemented acquire the data for a single line before reversing the current.[22] In our case, we can eliminate drifts on short time scales (<1 s). This is an advantage of the point-by-point method, especially when trying to measure small changes in the ECP. Note that line-by-line acquisition is different from *a posteriori* line-by-line mean value subtraction. On the other hand, line-by-line current reversal has an advantage of quicker line acquisition as the waiting time for thermal stabilization can be reduced to once per line. Acquiring full images for each current direction involves extensive post-processing to remove drifts and suffers from other problems in tip changes. It is therefore not considered to be a viable method.

Still, the dc mode is sensitive to dc voltage offsets in the setup, and it is important to zero them appropriately before starting the measurement [Eq. (6)]. Particularly important is an offset in the ADC or transimpedance amplifier since in order to compensate this offset, the feedback applies an additional voltage, which creates an offset current I_{off} in the junction, which contributes to the overall noise [Eq. (6)]. Therefore, we undertake a series of steps to ensure that all offsets are adjusted to zero before proceeding with the measurement. First, the ADC input offset is adjusted such that when no voltage is applied to the ADC input, its reading is zero. Finally, if the absolute value of I_s is not the same for the opposite current directions upon ECP and thermal extraction [Eqs. (23) and (24)], a crosstalk between the ECP and thermal channels can be induced. Therefore, we adjust the values of I_s for both current directions such that they are exactly equal in magnitude by using a resistor circuit [Fig. 1(c)], i.e., measuring I_t for the opposite directions of I_s. A drift in the voltage source (DAC2) controlling the current source, however, will in time cause slight differences between the positive and negative directions, which needs to be checked regularly. In general, having stable electronic components is very important for dc mode STP implementations.

Sample heating increases quadratically with I_s, thus becoming significant for higher current densities. Above a certain current density that depends on the resistivity and the thermal expansion coefficient of the sample, even fast polarity switches require a long waiting time before the sample temperature stabilizes. This significantly prolongs the measurement time and limits the dc mode to a maximum current.

B. ac mode

In the ac mode, the sample current oscillates with a frequency f_0 [Fig. 6(d)], $I_s = I_{s,0}\cos(2\pi f_0 t)$. This creates an oscillatory ECP at the position of the tip with the same frequency. We compensate the ECP to zero by applying an additional ac voltage $V_c\cos(2\pi f_0 t)$. The sampled tunneling current signal is fed into a lock-in amplifier for demodulation. With a phase shifter, the relative phase φ between I_s and V_c is adjusted so that they are in-phase at the position of the tip. Now, we can just consider the amplitudes of the signals as $\varphi = 0$. The total ac tunneling current is contained within $I_{\text{ac, X}}$, as we set the lock-in phase so that $I_{ac,Y} = 0$. Therefore, we can use $I_{\text{ac, X}}$ as an input for the ECP-feedback. The output of the ECP-feedback in the ac mode is then modulated with the same frequency f_0 as I_s and added to V in order to compensate the ac component of I_t to zero.

To achieve stable thermalization, we keep I_s on throughout the entire measurement. Meanwhile, V_c is within a few mV of the ECP value in order for I_{ac} to stay small and not interfere with the STM scanning. A block diagram of the acquisition of one data point in the ac mode is shown in Fig. 10. First, we apply $I_s > 0$, and as soon as the tip–sample separation is stable (sample well thermalized), we freeze the z-feedback and set $V_{scan} = 0$. Then, the ECP-feedback is activated to precisely adjust V_c such that $I_{\text{ac,X}}$ is zero. We wait a short time usually about five time constants of the lock-in low-pass filter for the feedback to settle and then start the acquisition of V_c (usually around 50–500 ms), which is exactly equal to μ_{ECP} (when $\varphi = 0$). Simultaneously, we acquire I_{dc}, which gives us $V_{th} = I_{dc}/R_t$. Using the setpoint value of R_t, here is an approximation as R_t can vary throughout the sample depending on the local $I_t(V)$ characteristic. A better way would be to have an additional controller to zero I_{dc} and thereby determine V_{th}, at the cost of making the measurement more complex. After the acquisition is complete, the ECP-feedback is disabled, V_{scan} is restored, and the tip moves on to the next point. The same as in the dc mode, we keep the ECP-feedback, i.e., ΔV_c, limited to a range of several mV around zero to prevent the feedback from overreacting to some transients and thus maintain tip stability throughout the measurement.

In contrast to the dc mode, the ac mode requires no current switches and it only requires properly matching the phases of the sample current and the sample bias to allow for ac signal

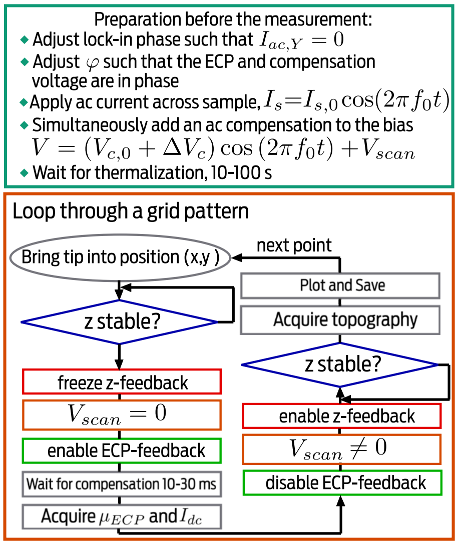

FIG. 10. A block diagram of a single point acquisition in the ac mode.

compensation. Furthermore, the ac mode is not susceptible to any offsets in the determination of the ECP even if offsets still play a role in measuring V_{th}. μ_{ECP} and V_{th} are effectively decoupled just by virtue of being measured at different frequencies, and hence, no further signal extraction is necessary. The sample heating is also smaller since the mean power of an ac signal is $1/\sqrt{2}$ of a dc signal of equivalent amplitude. Therefore, the ac mode can be performed with higher current densities without running into thermalization issues.

We choose $f_0 = 833$ Hz to perform measurements in the ac mode even though our transimpedance amplifier has nominally a 5 kHz bandwidth because we observe an increase in the spectral noise density of the transimpedance amplifier when connecting it to the coaxial cables, leading to the STM tip in the range from 1–5 kHz. This is a known phenomenon that the transimpedance amplifier input noise increases for higher frequencies due to the source capacitance and resistance.[20] We further note that in our implementation, the output amplitude V_c was updated by the feedback controller on an average time scale of 0.1 ms.

V. COMPARISON OF DC VS. AC MODE

A. Resistor circuit

In order to compare the performance of the ac and dc modes, we first use a simple resistor circuit [Fig. 1(c)] with $R_1 = R_2 = 1$ kΩ and $R_t = 100$ MΩ and $R_t = 1$ GΩ. We determine μ_{ECP}^{rms} as the standard deviation (Gaussian rms width) of 1024 points acquired consecutively with the same averaging time per point. Note that the averaging time t_{avg} used for the dc mode is given as twice the averaging time spent for each current direction. The dependence of μ_{ECP}^{rms} on t_{avg} for $R_t = 100$ MΩ and $R_t = 1$ GΩ is shown in Figs. 11(a) and 11(b). As expected, μ_{ECP}^{rms} reduces with increasing t_{avg}, i.e., the narrowing of the averaging filter bandwidth. However, the slope of the curves $\sim t_{avg}^{-\beta}$ differs substantially between the ac and dc modes. The slope for the ac mode is around $\beta \approx 1/2$ as expected for a flat noise spectrum. However, for the dc mode, $\beta \approx 0.2$, which indicates a strong flicker noise contribution. We also observe differences between $R_t = 100$ MΩ and $R_t = 1$ GΩ for the two modes. For $R_t = 1$ GΩ, the ac mode has lower μ_{ECP}^{rms} only for $t_{avg} > 300$ ms, whereas for $R_t = 100$ MΩ, the ac mode is better already for $t_{avg} > 100$ ms. We ascribe this observation to the flicker noise component in the surface potential in the dc mode, which presents itself more prominently for lower R_t as the other main noise contributions (junction and transimpedance amplifier) decrease with decreasing R_t and thus the surface potential contribution starts dominating. On the other hand, the ac mode has a higher noise for short integration times even though it is free of flicker noise. μ_{ECP}^{rms} in the ac mode corresponds well with the theoretically predicted values of 5 μV for $R_t = 100$ MΩ but is significantly higher (40 μV) for $R_t = 1$ GΩ, where the predicted value is around 30 μV (Fig. 7). In the dc mode, μ_{ECP}^{rms} shows a significant deviation from the Gaussian noise predictions (Fig. 3) due to flicker noise.

Increasing the averaging time and thus reducing the bandwidth of the measurement, we can finally reach an rms noise of about 1 μV for the ac mode with $R_t = 100$ MΩ and $t_{avg} = 4$ s. On the other hand, long t_{avg} increases the overall acquisition time substantially and makes the measurement procedure susceptible to electronic and thermal drifts on longer time scales. We discuss the latter issue in more detail in Sec. V C.

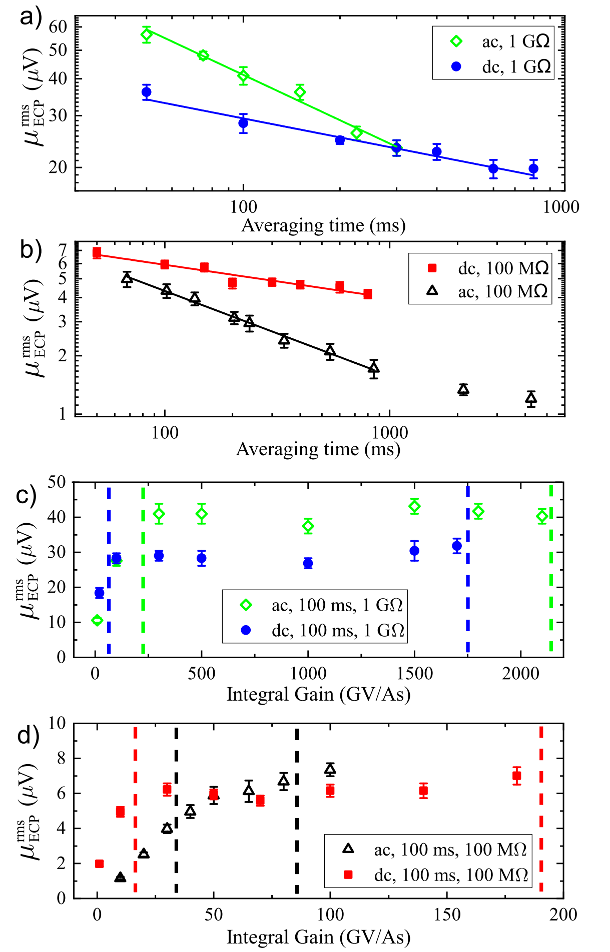

FIG. 11. (a) and (b) Dependence of μ_{ECP}^{rms} on the averaging time for (a) $R_t = 1$ GΩ and (b) $R_t = 100$ MΩ. The lines show a least-squares linear fit with a slope for the ac mode of -0.47 ± 0.01 for 100 MΩ and -0.51 ± 0.03 for 1 GΩ. For the dc mode, the slopes are -0.17 ± 0.02 for 100 MΩ and -0.21 ± 0.02 for 1 GΩ, indicating a strong flicker noise contribution. [(c) and (d)] Dependence of μ_{ECP}^{rms} on the integral gain for (c) $R_t = 1$ GΩ and (d) $R_t = 100$ MΩ, both with a 100 ms averaging time. The range between the vertical dashed lines indicates the integral gains for which the controller manages to compensate the input well, yielding a nearly constant μ_{ECP}^{rms}. For integral gains below the left boundary, the controller is reaching compensation asymptotically slow and the bandwidth is essentially dominated by the feedback controller. Above the right boundary, the controller output starts to oscillate. In this case, there is an extremely sharp increase in μ_{ECP}^{rms} (not shown). Interesting to note is that the range of the ac mode is higher than for the dc mode for $R_t = 1$ GΩ, but the opposite is true for $R_t = 100$ MΩ. Measurements for both modes were taken with $I_s = 1$ mA and a fifth order Butterworth low-pass filter with a cut-off frequency of 500 Hz. In the ac mode, the measurement frequency was $f_0 = 833$ Hz.

We have measured the dependence of μ_{ECP}^{rms} on the integral gain K_i of the controller, as shown in Figs. 11(c) and 11(d). For low K_i (left from the vertical dashed lines), we see a sharp drop in μ_{ECP}^{rms}. We ascribe this behavior to the controller, which is reacting asymptotically slow to the input, i.e., not compensating, which is in accordance with the model in Fig. 4. Between the vertical dashed lines, the controller compensates the input well and μ_{ECP}^{rms} is constant. Right from the vertical dashed lines, μ_{ECP}^{rms} increases very sharply as the controller output starts to oscillate [not shown in Figs. 11(c) and 11(d) to maintain the scale]. This is again in agreement with the model presented in Fig. 4. We can see that for R_t = 100 MΩ, the ac and dc modes give similar results, whereas for R_t = 1 GΩ, the ac mode shows significantly higher noise for the same t_{avg}. The reason for this observation can be found in the interplay between the generally larger rms noise of the ac mode and the flicker noise being more prominent in the dc mode at lower R_t in comparison to the other noise sources.

B. Graphene

The early implementations of STP were mostly used to measure electrical transport on thin metallic films deposited on insulating substrates. A common difficulty was maintaining the tip stability mainly due to the rough morphology of the films.[23] Recently, epitaxially grown graphene samples emerged as an ideal substrate for STP studies.[10,24–27] Therefore, we choose graphene mono- and bilayer samples to test the performance of our implementation.

Graphene is epitaxially grown on a commercial SiC–6H semi-insulating substrate (MSE supplies, thickness 330 μm, resistivity $> 1 \cdot 10^5 \Omega\,$cm) by thermal decomposition in ultra-high vacuum.[28] The sample is contacted *ex situ* by pressing indium foil with a thickness of 127 μm onto the SiC wafer using Ta clamps to achieve a direct contact to graphene. This creates a reasonably good contact resistance (~ 100 Ω) without the need of any *ex situ* evaporation that could contaminate the sample. After reintroduction to ultra-high vacuum, the sample is degassed at about 100 °C for 30 min to remove adsorbates. The sample is predominantly covered by bilayer graphene and smaller areas with monolayer graphene. We used an electrochemically etched W tip[29] prepared *in situ* by Ar sputtering and electron beam annealing. The tip was checked by STM scanning and $I_t(V)$ curve acquisition on a clean Au(111) surface to verify its quality before proceeding to measure the graphene sample. An important indicator of good tip quality for ECP measurements was a stable linear $I_t(V)$ characteristic on Au(111).

Figure 12 shows simultaneously acquired topography, ECP, and thermal voltage images for both the [(a)–(c)] dc and [(d)–(f)] ac modes. The measurements were recorded across 500 nm on the same epitaxial graphene sample with the current flowing in the horizontal direction (current density 4 A/m). The measurements in both modes were done at room temperature using the same setpoint conditions (50 mV, 500 pA) with a setpoint resistance of R_t = 100 MΩ and t_{avg} = 200 ms per point.

The topography of graphene acquired in the dc mode is shown in Fig. 12(a) where the steps correspond to the substrate steps of the underlying SiC and monolayer-bilayer graphene steps.[28] A cross section is shown in the lower half of each sub-figure of Fig. 12. The ECP has a clear drop across the sample in the direction of the current [Fig. 12(b)], corresponding to a graphene sheet resistance of (170 ± 10)Ω. Note that the found sheet resistances are a factor of 2–3 lower than reported previously,[27] which indicates a substantial bulk conductance of the SiC substrate. The cross section is taken across a part covered entirely by bilayer graphene. The bright lines in the thermal voltage image in Fig. 12(c) are characteristic features of bilayer graphene films on SiC.[30] Monolayer graphene is free of the lines in the thermal voltage map as can be seen on the slightly brighter, line-free patches marked by the red arrows in the image in Fig. 12(c).

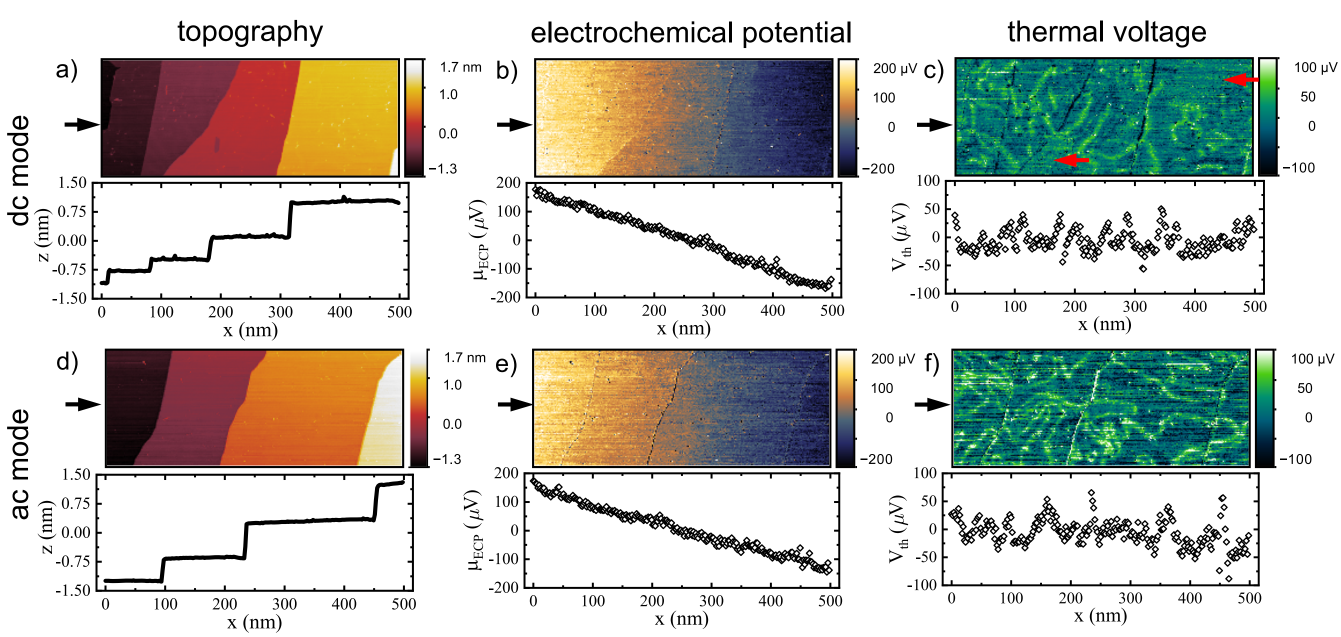

FIG. 12. Simultaneously acquired (a) and (d) topography, (b) and (e) μ_{ECP}, and (c) and (f) V_{th} for both dc and ac mode STP implementations. A horizontal cross section is shown below each image, with the position marked by a black arrow on the left-hand side of the image. Each cross section was obtained by averaging five image lines. Settings for topography (bias 50 mV, tunneling current 500 pA, acquisition time 10 ms); averaging time for μ_{ECP} and V_{th} is 200 ms per point.

For the ac mode, the topography is shown in Fig. 12(d) with the steps in topography corresponding only to the SiC substrate steps as the entire image area is covered by bilayer graphene. Note that in the ac mode, the topography is also acquired with a dc gap voltage, but with a nearly compensated ac bias current. Again, we see a characteristic slope in the ECP map corresponding to a sheet resistance of $(140 \pm 10)\Omega$ in Fig. 12(e). The thermal voltage map shows again the domain lines that are characteristic for bilayer graphene. It should be noted that the thermal voltages shown in Figs. 12(c) and 12(f) are not exactly equivalent. The thermal voltage in the dc mode is extracted from the compensation voltages for both current directions. In the ac mode, we measure the residual dc current I_{dc} when the gap voltage is set to zero and calculate the thermal voltage $V_{th} = I_{dc}/R_t$ by assuming that the local tunneling resistance is equal to the setpoint resistance R_t, which is only approximately correct. Comparing the two thermal voltage images in Figs. 12(c) and 12(f), we see that the thermal maps agree reasonably well.

Both modes give a clear topographical image comparable to what we obtain by scanning on the same sample in the absence of a bias current. Imaging in the ac mode appears somewhat better, probably due to the fact that current switching is not necessary and therefore a more stable sample temperature is achieved, although this can also be a consequence of a slightly different tip preparation between the two images. Comparing the ECP measurements in Figs. 12(b) and 12(e), we find very similar maps with slightly different potential slopes due to different sample areas being measured. The cross sections reveal in both the dc and ac modes about the same noise of about 20 μV with both modes being able to resolve features in the ECP on the order of 10 μV. Two prominent steps in the dc mode ECP image in Fig. 12(b) can be seen at the monolayer-bilayer boundary corresponding to a defect resistance of about 10 $\mu\Omega$ m^{-1}, which is in agreement with previous studies.[10,25–27] In the thermal voltage images in Figs. 12(c) and 12(f), we see similar variations of around 80 μV in both the dc and ac modes between the bilayer lines and the bilayer background. From this, we can conclude that there was no significant difference in sample heating in the two modes.

For the same current of 1 mA that was used with the resistor box measurements (Fig. 11), we measure $\mu_{ECP}^{rms} = (12.4 \pm 0.5)\ \mu$V and $\mu_{ECP}^{rms} = (9.8 \pm 0.3)\ \mu$V for the ac and dc mode, respectively, when measuring on a 1 nm^2 area (1024 points) of graphene. μ_{ECP}^{rms} is higher than the resistor circuit result of around 6 μV for the same $t_{avg} = 100$ ms. This discrepancy can be due to several factors. The most important one is the tip–sample distance, which can be influenced by vibrations in the junction and thermal drift. This shows that the effect of the variation in tip–sample distance should be considered thoroughly when attempting to reach sub-μV resolution in ECP measurements.

It is not straightforward to directly compare the noise performance of our STP implementation to others[6–11] since the exact averaging time per data point is not specified. Despite that, we can give a rough comparison based on the overall time necessary for the entire image acquisition. If we assume a similar ratio between waiting time and averaging time as we have in our experiment, we conclude that our performance in terms of the signal-to-noise ratio is comparable to the most recent STP implementations[8,11] where a resolution of around 10 μV was demonstrated.

C. Effects of thermalization

Increasing the current in the dc mode also requires increasing the stabilization delay time in order to reach thermal equilibrium between the current direction switches. The stabilization time increases faster than linear with the sample current because the heating power scales quadratically with current. At some point, the stabilization delay time becomes impractically long (>100 ms), which leads to long measurement times and other problems, i.e., drifts in the x and y direction and long term drifts of the electronic outputs. On the other hand, if we do not increase the delay time appropriately, a crosstalk between the thermal voltage and ECP signals starts appearing for larger current densities (Fig. 13). This crosstalk is due to a small difference in sample temperature (<1 K) between the positive and negative current data acquisition. Ultimately, the reason lies in the way we extract the ECP and thermal voltage from the compensation voltage measured for both positive and negative current directions. In the thermal map of Figs. 13(a) and 13(b), we see a ring-like feature in the lower right corner. This feature is also reflected in the ECP image in Fig. 13(b) (red arrow). The crosstalk is about 20–30 μV, which is significant when pursuing sub-μV STP resolution.

The current switching also leads to repeated heating–cooling cycles, which correspond to thermal expansion–contraction cycles of the sample. The expansion–contraction cycle becomes prominent for large currents (>50 pm for this particular sample with $I_s > 3$ mA), and can lead to instabilities in the tip–sample junction and ultimately to the tip crashing into the sample. A way to address this thermalization problem in the dc case is to perform the current switching line by line, as discussed in Subsection IV A. Another way is to minimize the sample contact resistance, as this is a local source of Joule heating.

The ac mode, on the other hand, does not suffer significantly from crosstalk between the ECP and thermal voltage channels because they are detected in different ways [Figs. 14(a) and 14(b)]: ECP as an ac signal and the thermal voltage as a dc signal. The ac current is also heating the sample less since the ac Joule heating scales with $I_s^2/2$. Moreover, the sample temperature adds an oscillatory component with frequency $2f_0$ to the thermal voltage [Eq. (22)]. After demodulation, the oscillatory part of the thermal voltage is shifted to f_0 and $3f_0$, and both of these components are efficiently removed by using the lock-in low-pass filter. Hence, the thermal voltage does not intermix in the ECP signal in the ac mode. However, this does not mean that the ac sample current can be increased indefinitely. Changes in the sample resistance, particularly due to the contact resistance changes during the scan, are very important since they effectively introduce a relative phase drift between the ECP and compensation voltage. This phase drift significantly increases the noise component proportional to I_{ac}. We can see this noise increase directly by comparing Figs. 14(a) and 14(b). Therefore, reducing the sample contact resistance is very important in the ac mode as well.

In practice, there are significant overhead times per point for each mode. In measuring the graphene sample with a 4 A/m current density, the overhead time in the dc mode was around 150 ms per point, whereas in the ac mode, it was around 40 ms, which is a significant practical advantage for the ac mode. Such a significant difference is due to stabilization waiting times after every current

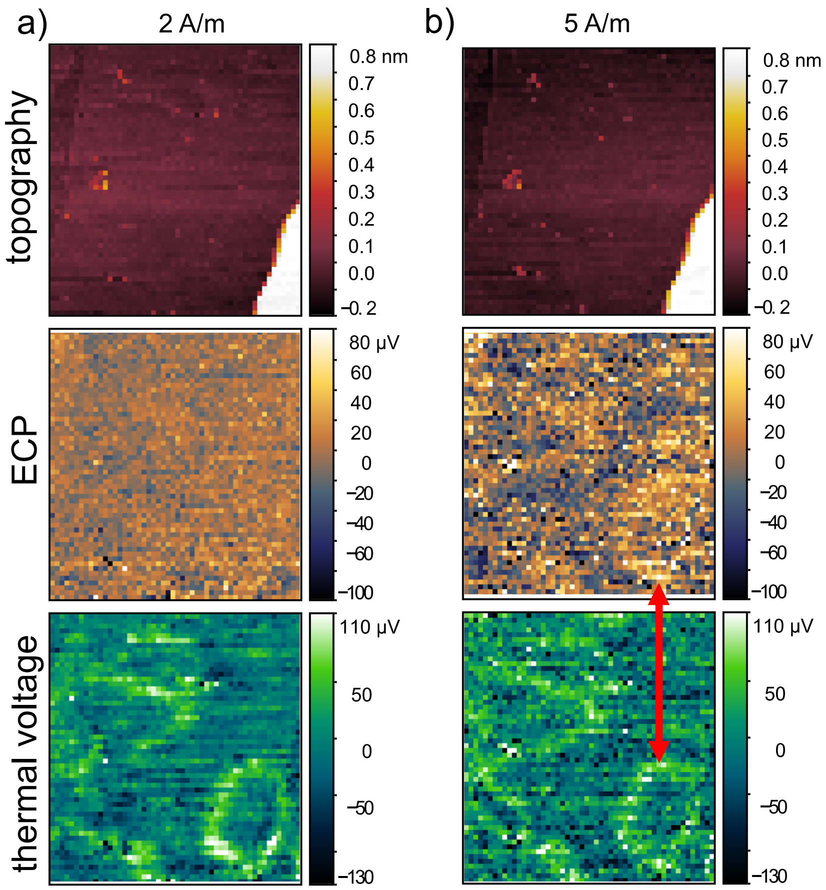

FIG. 13. Topography, ECP, and thermal voltage maps simultaneously acquired in the dc mode for a current density of (a) 2 A/m and (b) 5 A/m. The width of each image is 70 nm. The linear slope has been subtracted from the ECP images in order to show the crosstalk feature more clearly. A ring-like feature can be observed in the lower right corner of the thermal voltage images in (a) and (b). However, in (b), we also see this feature reflected in the ECP image (red arrow). The thermalization delay of 70 ms is the same in both images.

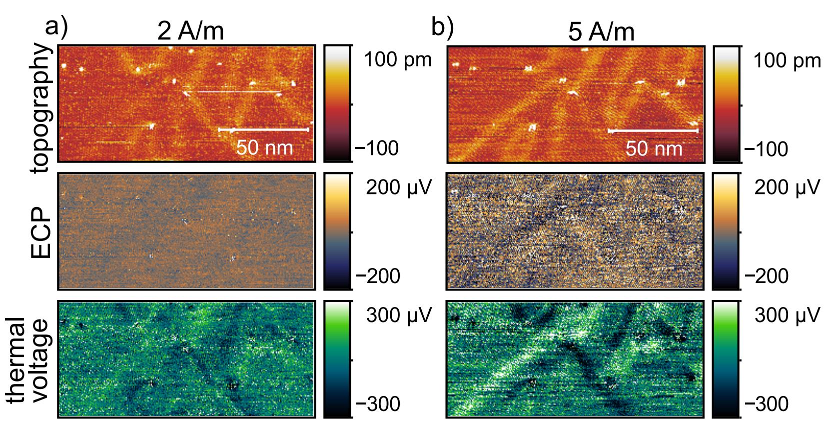

FIG. 14. Topography, ECP, and thermal voltage maps simultaneously acquired in the ac mode for a current density of (a) 2 A/m and (b) 5 A/m. A scale for the images is given in the topography images. The linear slope has been subtracted from the ECP images in order to show the noise increase with current more clearly.

direction switch in the dc mode. In the ac mode, the waiting time is mainly defined by the lock-in effective cut-off frequency f_c where we usually wait for 5–10 filter time constants $\tau = 1/f_c$ for the feedback output to settle.

VI. CONCLUSIONS

We have presented a complete noise analysis of STP applicable to all the different experimental modes whether they are dual-feedback or sample-and-hold, dc or ac. Our analysis highlights two primary noise sources: the tunneling junction thermal noise and the transimpedance amplifier input noise. Additionally, we have demonstrated that secondary noise sources such as the surface potential noise, mainly determined by the compensation voltage source and different electronic offsets, can also play a crucial role and even dominate the noise spectrum in certain cases. The flicker noise plays a significant role in the dc mode but can be completely removed by using the ac mode, however, at the cost of a factor $\sqrt{2}$ higher baseline noise. Furthermore, we have considered the impact of the feedback on the compensation voltage and have shown that a PI controller is not ideal to measure samples with large variations in the local $I_t(V=0)$ characteristics. Such a detailed noise analysis is necessary to achieve sub-μV resolution in STP measurements.

A significant factor in implementing STP measurements is to use a low-noise versatile electronics that allows for the implementation of the different measurement modes fully by software. With the progress in STM electronics, we envision that the implementation of scanning probe modes such as STP will become significantly easier. We have implemented STP in a sample-and-hold approach, with both dc and ac modes in our STM setup fully by software. We performed measurements both on a model resistor circuit and on epitaxial graphene to directly compare the dc and ac mode. Both modes have their advantages and disadvantages. The dc mode requires fast current direction switches with simultaneous tunneling gap voltage changes in order to measure at suitable sample currents without long stabilization delays. These switches make the implementation of this mode complicated, although the dc mode theoretically has a lower noise than the ac mode when the flicker noise is negligible. Our point-by-point current switching measurement scheme ensures that no post-processing is needed for extracting the ECP and thermal voltage signal, thus minimizing possible artifacts and ensuring good correlation between the topography and ECP data. The electronic offsets have to be carefully compensated in the dc case to achieve optimal noise performance. On the other hand, implementing the ac mode requires the use of a lock-in amplifier, which, in our case, is integrated into the electronics, but still adds to the complexity of the implementation. Both measurement modes show comparable performance on the resistor circuit and on epitaxial graphene, with both being able to resolve sub-10 μV steps in ECP with 200 ms averaging time per point. The comparable performance is due to the fact that even though the dc mode has nominally lower noise, our setup suffers from a strong flicker noise contribution, which raises the dc noise and makes it comparable to the nominally higher noise level of the ac mode.

ACKNOWLEDGMENTS

We thank Peter Märki and Yves Acremann for insightful discussions on low-noise electrical measurements. We also thank Kenneth Kollin for help with the control electronics programming. We acknowledge funding from the Swiss National Science Foundation, Project No. 200021_163225. H.W. was supported by the China Scholarship Council (CSC) under Grant No. 201806340092.

AUTHOR DECLARATIONS

Conflict of Interest

The authors have no conflicts to disclose.

DATA AVAILABILITY

The data that support the findings of this study are available from the corresponding author upon reasonable request.

APPENDIX A: BASICS IN NOISE ANALYSIS

In this appendix, we will present general expressions and equations that are used in noise analysis. A common type of noise is the so-called Gaussian (white) noise, which means that the values of a signal are distributed according to the Gaussian probability function around a mean value b with a certain variance c^2,

$$f(x) = a\exp\left[-\frac{1}{2}\frac{(x-b)^2}{c^2}\right]. \tag{A1}$$

Within a range of $[b-3c, b+3c]$, we find about 99.73% of the signal values. We consider this range as the peak-to-peak (p–p) noise value. If the mean value b is zero, the standard deviation c of the signal will be equal to the root-mean-square (rms) value. Thus, we can relate the values as

$$6\cdot V_{noise,rms} = V_{noise,p-p}. \tag{A2}$$

The Gaussian noise is spectrally flat; however, in a real signal, there can be significant deviations from that. Therefore, it is useful to define the power spectral density (PSD), which describes how the power of a signal is distributed over a frequency range. In order to calculate the noise PSD, we perform a Fourier transform of a signal $x(t)$, which has a zero mean value $[\hat{x}(f) = \int_{-\infty}^{\infty} x(t)e^{-2\pi f j t}\mathrm{d}t]$, where j is the imaginary unit, f is the frequency, and t is the time. To obtain the PSD S_x of x, one has to multiply the noise current spectrum $\hat{x}(f)$ with its complex conjugate $\hat{x}^*(f)$,

$$S_x = \hat{x}(f)\hat{x}^*(f). \tag{A3}$$

For a current signal, the noise PSD has the units of A^2/Hz. As an example, let us look at a typical tunneling current noise PSD, which is schematically shown in Fig. 15. Starting from 0 Hz up to a corner frequency f_F, flicker noise dominates the spectrum. Flicker noise is inversely proportional to the frequency. The middle frequency range from f_F to the cutoff frequency of the amplifier f_{amp} is flat and, therefore, white Gaussian noise. The amplifier has a cutoff frequency f_{amp}, so the noise at higher frequencies than that is suppressed. In a real experiment, there will also be additional noise contributions from mechanical tip–sample variations that can be broad or peaked in frequency and specific noise peaks of electronic origin due to the environment (ground loops and electromagnetic radiation).

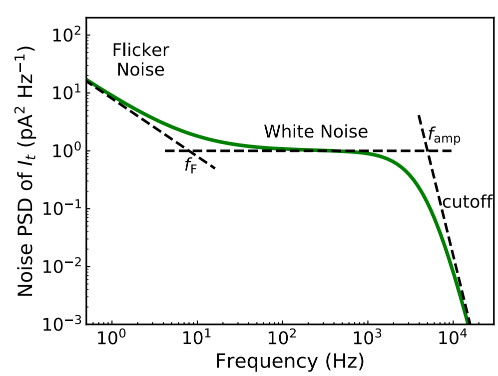

FIG. 15. A typical noise power spectral density (noise PSD) spectrum of the tunneling current noise in an STM measurement. This assumes that the STM is extremely stable (no mechanical vibration peaks in the spectrum) and free of any electromagnetic interference (no electromagnetic interference peaks in the spectrum).

The total noise PSD S_{tot} of two voltage noise sources with noise PSD S_x and S_y is

$$S_{tot} = (\hat{x}(f) + \hat{y}(f))\,(\hat{x}(f) + \hat{y}(f))^* = S_x + S_y + \hat{y}(f)\,\hat{x}(f)^* + \hat{x}(f)\,\hat{y}(f)^*. \tag{A4}$$

When x and y are independent of each other, the two cross correlation terms $\hat{y}(f)\,\hat{x}(f)^*$ and $\hat{x}(f)\,\hat{y}(f)^*$ are zero, i.e., different instances of $x(t)$ and $y(t)$ will yield on average a vanishing cross correlation. Finally, the procedure to add multiple independent noise sources follows analogously,

$$S_{tot} = \sum_i S_i. \tag{A5}$$

Therefore, to obtain the total rms noise of several independent sources, we just have to add all the spectral noise densities together, integrate them over the bandwidth BW, and take a square root of the obtained result,

$$x_{rms} = \sqrt{\int_0^{BW} S_x\,\mathrm{d}f} = \sqrt{\int_{-BW}^{+BW} S'_x\,\mathrm{d}f}. \tag{A6}$$

We denote S_x as the one-sided PSD function and S'_x as the two-sided PSD. Furthermore, we continue using the one-sided PSD since most real-world instruments display only the positive half of the frequency spectrum since real signal PSDs are symmetrical around 0 Hz. In order to convert a two-sided PSD, we discard the negative frequency part of the spectrum and multiply all positive frequency PSD amplitudes by 2. Note that the PSD at 0 Hz is not multiplied by 2.

APPENDIX B: NOISE IN THE TUNNELING JUNCTION

The noise in the tunneling junction has three distinct contributions: the Johnson–Nyquist thermal noise, the shot noise, and the noise due to the difference in temperature between the tip and the sample.[31] The Johnson–Nyquist thermal noise PSD is given by

$$S_{Johnson} = \frac{4k_B T}{R_t} \tag{B1}$$

and is present always for a non-zero junction temperature. On the other hand, shot noise arises exclusively when there is current flow in the junction,

$$S_{Shot} = 2e|I|, \tag{B2}$$

where $|I|$ is the average current in the junction and e is the electron charge. In STP, in the dc mode, the dc tunneling current is compensated to zero in which case the contribution of the shot noise can be disregarded. However, a finite I_{off} [Eq. (6)] can lead to an appearance of the shot noise term in the tunneling junction. A reasonable estimate is that we can experimentally easily adjust the offset to below $V_{\mathrm{off}} = 0.1$ mV, which leads to a tunneling current $I_{\mathrm{off}} = V_{\mathrm{off}}/R_t$, which for a range of $R_t = 10$–$1000\ \mathrm{M}\Omega$ is $I_{\mathrm{off}} = 0.1$–10 pA. The range of I_{off} corresponds to a shot noise PSD of $S_{Shot} \approx 3 \cdot 10^{-30}$–$3 \cdot 10^{-32}$ A^2/Hz. Even for the smallest $R_t = 10\ \mathrm{M}\Omega$ where the shot noise contributes the largest, it is still an order of magnitude below $S_{Johnson}$ at room temperature and, therefore, insignificant. At low temperatures $T = 15$ K, the shot noise becomes comparable to the Johnson noise.

The noise PSD term due to the temperature difference between the tip and the sample is

$$S_{\Delta T} = \frac{1}{4}\left(\frac{\pi^2}{9} - \frac{2}{3}\right)\left(\frac{\Delta T}{\overline{T}}\right)^2 2k_B \frac{\overline{T}}{R_t}, \tag{B3}$$

where ΔT and $\overline{T}$ are the difference and arithmetic average between the tip and sample temperatures, respectively. The term $S_{\Delta T}$ scales with the average Johnson–Nyquist noise $4k_B\overline{T}/R_t$ and $(\Delta T/\overline{T})^2$. In case when the sample and tip are not intentionally heated, the current flow through the sample can create a temperature difference of a few K. Therefore, $S_{\Delta T}$ is proportional to $S_{Johnson}$ with a factor $(\pi^2/9 - 2/3) \cdot (\Delta T/\overline{T})^2/8 \approx 1 \cdot 10^{-7}$ for $\overline{T} = 300$ K and $(\Delta T/\overline{T})^2 \approx 1 \cdot 10^{-3}$ for $\overline{T} = 15$ K.

The dominant term in the tunneling junction noise in STP is, therefore, the Johnson–Nyquist noise, and we represent the junction noise as consisting only of a Johnson–Nyquist contribution in all the calculations,

$$S_j = S_{Johnson} + S_{Shot} + S_{\Delta T} \approx S_{Johnson} = \frac{4k_B T}{R_t}. \tag{B4}$$

APPENDIX C: TRANSFER FUNCTIONS

Besides the spectral noise density, the other parameter that determines the total noise is the measurement bandwidth (BW). The bandwidth of a system is determined by its frequency response $|F(f)|$. The frequency response is defined as the amplitude of the transfer function $F(f) = |F(f)|e^{\arg(F(f))}$ where the transfer function is a mathematical function that describes a systems' output for any possible input and arg is the argument of a complex number, i.e., the angle between the positive real axis and the line joining the origin and the complex number in the complex plane. A straightforward way to understand the effect of the filter transfer function on a signal is to take as an input $\cos(2\pi ft)$, which results in an output $|F(f)|\cos(2\pi f t + \arg(F(f)))$. Therefore, an input with frequency f gets scaled by $|F(f)|$ and phase shifted by $\arg(F(f))$. Since any input signal can be decomposed into its frequency spectrum, the shape of the frequency response $|F(f)|$ in the frequency spectrum directly determines which frequencies get attenuated and which get amplified. We obtain the noise power as

$$P_{noise} = \int_0^{+\infty} S_x(f)|F(f)|^2\,\mathrm{d}f. \tag{C1}$$

To obtain the noise rms value, we simply take the square root of the calculated noise power. Finally, the bandwidth is defined as

$$BW = \int_0^{+\infty} |F(f)|^2\,\mathrm{d}f. \tag{C2}$$

We can actually obtain the transfer function of a system by solving its differential equation using the Laplace transform $H(s) = \int h(t) \cdot e^{st}\,dt$. The frequency and phase response are obtained easily by setting $s = j2\pi f$, where j is the imaginary unit and f is the frequency.

APPENDIX D: ANALYSIS OF THE CLOSED-LOOP BEHAVIOR

At this point, we discuss the impact of the ECP-feedback controller on the overall performance of the STP measurement. Many different feedback controllers for continuously operating dynamical systems exist. One of the most well-known and widely used controllers is the proportional-integral PI controller, and we will focus the analysis on this controller type. The controller output u (control signal) is determined from its input e (error signal) by the following equation:

$$u(t) = K_p e(t) + K_i \int_0^t e(t')dt', \tag{D1}$$

where K_p and K_i are the proportional and integral gain factors, respectively. We proceed directly with the PI controller transfer function

$$H_C(s) = K_p + \frac{1}{s}K_i \tag{D2}$$

and its frequency response

$$|H_C(f)| = \sqrt{K_p^2 + K_i^2/(2\pi f)^2}. \tag{D3}$$

More details on how to obtain the transfer function of a differential equation and its frequency response are given in Appendix C.

We use the schematic representation of the STP experiment shown in Fig. 16 to find its closed-loop transfer function. We are interested in the reaction of the output u to a change in v. The signal u represents the measured ECP, and v is the surface potential that arises from the bias current flow. The reference r is the controller setpoint, which, in our case, is set to zero to which the output current i (voltage representation of the tunneling current in the electronics) is referenced. The error current $e = r - i = -i$ is the input signal that the controller has to minimize. We use the term n to quantify the noise in the system. We will first discuss the behavior of the control system with $n = 0$. Calculating the reaction in u to changes in v is equivalent to moving the STM tip along the surface to locations with the different local ECP or changing the bias current. The total gap voltage is $o = u + v$, and the total tunneling current is given by $i = Po$.

The transimpedance amplifier has a specific frequency response, which resembles a low-pass filter; see Fig. 15. When the frequency response of the digital filter has a lower cut-off frequency than the transimpedance amplifier, the overall behavior of process P is dominated by using the digital filter (Fig. 17). Otherwise, the two filters have to be considered separately. However, in our experiment, the low-pass filter cut-off frequency is always lower than the amplifiers. Hence, we can proceed by considering only the digital filter frequency response. To calculate the noise PSD through the process, we note that the fluctuations of the surface potential n_v are first transduced by R_t, before the junction noise n_j and equivalent current input noise of the TIA n_a get added to it. Thereafter, the associated noise currents get amplified by k, and eventually, the input noise of the ADC is added S_{ADC}. The PSD resulting from this process is

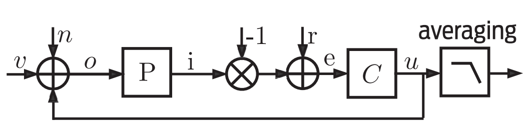

FIG. 16. Block diagram of the control system. C is the PI controller and P is the process. P represents the conversion of a surface potential with respect to the tip into a voltage read by the electronics. The reference $r = 0$ is the setpoint of the controller, $e = r - i = -i$ is the error signal, and i is the output current. Signal u is the controller output, i.e., the measured ECP signal after further averaging, v, is the voltage that arises in the sample due to the bias current and o is the total voltage applied to the sample. All the noise in the measurement is quantified by the term n.

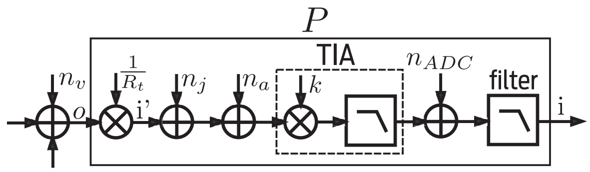

FIG. 17. Block diagram describing in detail the process P from Fig. 16. The process P consists of the tunneling junction, transducing the surface potential v via R_t into I_t, which is amplified by a gain k via a transimpedance amplifier (TIA) and subsequently sampled by using an ADC before entering a low-pass filter. Various noise contributions enter the process at different points, where n_v is the surface potential fluctuations, n_j is the junction noise, n_a is the TIA input noise, and n_{ADC} is the ADC input noise.

$$S_P = k^2\left(\frac{S_v}{R_t^2} + S_j + S_a\right) + S_{ADC}, \tag{D4}$$

whereas the process frequency response would be

$$P = \frac{k}{R_t}F, \tag{D5}$$

where F is the transfer function of the low-pass filter. Now, if we want to represent the total PSD of the process P with only one equivalent noise term n at the position of n_v, it would be $S_n = S_P \cdot R_t^2/k^2$. The factor R_t/k effectively transforms the current noise into an apparent surface potential noise, which is the relevant quantity in our measurements.

Making use of the system equations

$$e = -i, \quad i = Po = P(u + v), \quad u = Ce, \tag{D6}$$

we find the closed-loop transfer function of the system relating input v to output u,

$$H_{PI} = -\frac{CP}{1 + CP}. \tag{D7}$$

In the real experiment, we use digital filters $F(f)$ different from a simple low-pass filter. The frequency response $|H_{PI}(f)|$ with a fifth order Butterworth filter with a cut-off frequency of 500 Hz is shown in Fig. 18(a). Besides the frequency response, which allows us to calculate the ECP rms noise, another important parameter is the step response [Fig. 18(b)], which indicates how quickly the system reaches the steady state following a sharp step in v. As shown in Figs. 18(a) and 18(b), the behavior of both the frequency and step response for a given R_t strongly depends on the integral gain K_i. For $K_i < 150$ GV/As, we have asymptotic behavior in the compensation of the voltage step. For $K_i > 900$ GV/As, we start getting oscillations in the response, and for $K_i > 1500$ GV/As, the amplitude of the oscillations increases in time, making the controller fully unstable. This

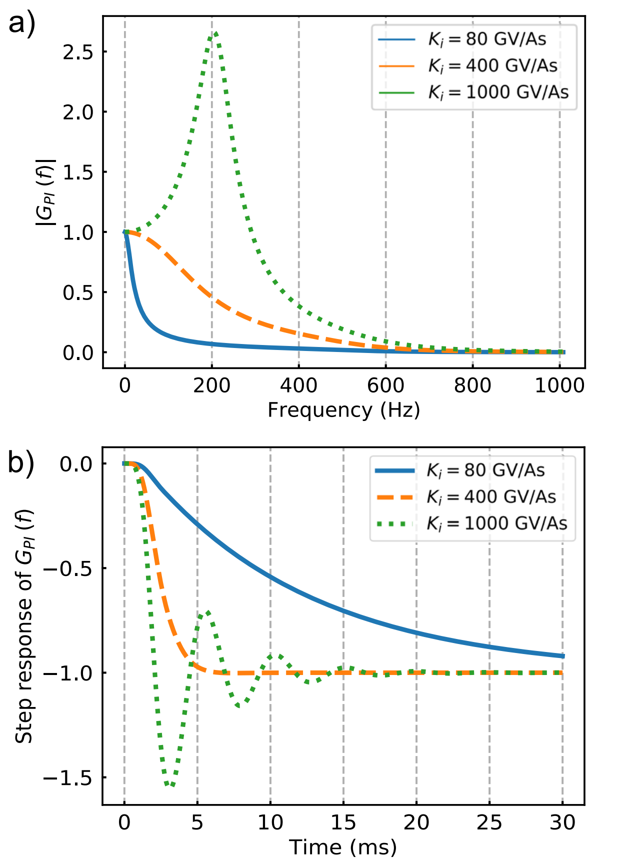

FIG. 18. Frequency (a) and step (b) response of the system H_{PI} in closed-loop configuration as a function of the integral gain K_i. R_t = 1 GΩ, K_p = 1 kV/A, and $k = 10^9$ V/A. The filter is a fifth order Butterworth filter with a cut-off frequency of 500 Hz.

demonstrates that there is an optimal value of K_i to choose in order to achieve a quick compensation of the surface potential.

We will further analyze the stability and steady-state error of the system. To simplify the formulas, we use a simple low-pass filter (first order RC) with its transfer function given as $F(s) = \omega_c/(s+\omega_c)$, where $\omega_c = 2\pi f_c$ and f_c is the filter cut-off frequency. The closed-loop transfer function is then

$$H_{PI}(s) = -\frac{K_i s + K_p}{\frac{R_t}{\omega_c k}s^2 + \left(\frac{R_t}{k} + K_p\right)s + K_i}. \tag{D8}$$

We can analyze the system stability by partial fraction decomposition of H_{PI} to find its poles and zeros,

$$H_{PI}(s) = \frac{b_1 s + b_0}{a_2 s^2 + a_1 s + a_0} = \frac{c_1}{s - p_1} + \frac{c_2}{s - p_2}, \tag{D9}$$

where p_1 and p_2 are the poles and the rest of the constants are real and positive. The poles are

$$p_{1,2} = -\frac{R_t + K_p k}{2R_t/\omega_c} \pm \sqrt{\left(\frac{R_t + K_p k}{2R_t/\omega_c}\right)^2 - \frac{K_i k}{R_t/\omega_c}}. \tag{D10}$$

Important for the stability of the feedback are the positions of the poles in the complex plane. If the poles are real and positive, the system is unstable and the response increases in time. On the other hand, negative and real poles will damp the response with the increasing absolute value of the pole. An imaginary part of the pole will result in an oscillatory behavior with the frequency increasing with the magnitude of the imaginary part. An oscillatory behavior occurs if the second term under the square root exceeds the first term,

$$(R_t + K_p k)^2 < \frac{4K_i k R_t}{\omega_c}. \tag{D11}$$

Thus, if K_i becomes too large for a given K_p and R_t, the system goes into oscillation, which is in accordance with Fig. 18. Furthermore, the condition for oscillations depends on both K_i and R_t, which implies that not all values of K_i and R_t lead to stable compensation. An important case is $K_p = 0$, for which we find $K_i > 0.25 R_t \omega_c / k$, i.e., a linear dependence of K_i on R_t. We can check the condition when one pole will be greater than zero,

$$-\frac{K_i k}{R_t/\omega_c} > 0. \tag{D12}$$

Since all parameters are positive, this condition is never fulfilled. Thus, the system is always stable when being out of the oscillatory response regime.

It is crucial for an STP procedure to precisely compensate the tunneling current to zero. The parameter quantifying this condition is the steady state error, which is defined as $e_{ss} = \lim_{t\to\infty} e(t)$. If the system is stable, we have

$$e_{ss} = -\lim_{s\to 0} \frac{sP}{1 + CP} v(s) \to 0 \tag{D13}$$

as long as K_i is finite. Therefore, there is no steady-state error in the closed-loop system, which is in accordance with Fig. 18.

Sampling for a time t_{avg} is equivalent to a moving average filter (Fig. 16), which has the frequency response

$$|F_{avg}(s)| = \frac{\sin(s t_{avg}/2)}{s t_{avg}/2} \tag{D14}$$

and a bandwidth of $BW_{avg} = 1/2t_{avg}$. Thus, we obtain Eq. (12).

Until now, we have neglected the discussion of the proportional gain parameter K_p. The closed-loop controller behavior appears relatively insensitive to the value of K_p. For low values of K_p, the feedback behaves purely as an integral controller. As can be seen from Eq. (D11), increasing K_p will result in an oscillatory response of the feedback; hence, we can drop the proportional feedback. The above analysis hints at the possibility that there may be better suited feedback controllers for the ECP measurements than the employed PI controller. Ideally, the system transfer function can react fast to current changes within the bandwidth of the transimpedance amplifier and can also cancel periodic noise at some particular frequencies of the system.

APPENDIX E: DERIVATION OF NOISE PSD FOR THE AC MODE

The phase of the lock-in amplifier is set such that all signal is in $I_{\mathrm{ac,X}}$ when using a finite ac bias current with little or no compensation. This is achieved by maximizing the capacitive coupling between bias and current line with the tip out of the junction and then rotating the phase by $\pi/2$. Starting from Eq. (4), we can calculate

$$\begin{aligned} I_{\mathrm{ac,X}} &= I_t(t)\cos(2\pi f_0 t) \\ &= [(I_{dc}+i_v(t))(1+\eta(t))+i_j(t)+i_a(t)]\cdot\cos(2\pi f_0 t) \\ &\quad + \frac{1}{2}(1+\eta(t))I_{ac}+\frac{1}{2}(1+\eta(t))I_{ac}\cos(4\pi f_0 t), \end{aligned} \tag{E1}$$

where we have used $\cos^2 x = (\cos 2x + 1)/2$. We multiply the following expression by 2 since the desired signal is equal to I_{ac}. All other components in the equation mentioned above are considered as noise to the ac current

$$\begin{aligned} i_{t,ac} &= I_{ac}(1+\eta(t))\cos(4\pi f_0 t)+\eta(t)I_{ac} \\ &\quad + 2[i_v(t)+i_v(t)\eta(t)+i_j(t)+i_a(t)]\cos(2\pi f_0 t) \\ &\quad + 2I_{dc}(1+\eta(t))\cos(2\pi f_0 t), \end{aligned} \tag{E2}$$

where we have introduced two terms I_{dc} and I_{ac}. I_{dc} is a term that represents a dc tunneling current in the junction. A dc current will have a contribution at frequency f_0 and can be difficult to filter out from the lock-in output if its magnitude is sizable. In the sample-and-hold implementation, we do not use a dc tunneling current for z-feedback control, i.e., the gap voltage is set to zero. Still, due to Joule heating of the sample by the bias current, a thermal voltage [Eq. (22)] proportional to the difference in temperatures between the tip and the sample arises and can take values up to a few mV depending on the sample current and resistance. The dc current resulting from the thermal voltage is $I_{dc} = V_{th}/R_t$.

Furthermore, we can again disregard the term η in comparison to 1 in Eq. (E2) for the i_v term for the same reasons as described for the dc mode. To proceed to the PSD of the noise in the ac mode, we take the Fourier transform of the ac current. We find that

$$\begin{aligned} \hat{i}_{t,ac}(f) &= I_{ac}\frac{1}{2}[\delta(f-2f_0)+\delta(f+2f_0)]+I_{ac}\hat{\eta}(f)+I_{ac}\hat{\eta}(f)*\frac{1}{2}[\delta(f-2f_0)+\delta(f+2f_0)]+[\hat{i}_v(f)+\hat{i}_j(f)+\hat{i}_a(f)] \\ &\quad *[\delta(f-f_0)+\delta(f+f_0)]+I_{dc}[\delta(f-f_0)+\delta(f+f_0)]+I_{dc}\hat{\eta}(f)*[\delta(f-f_0)+\delta(f+f_0)] \\ &= I_{ac}\hat{\eta}(f)+(\hat{i}_v(f-f_0)+\hat{i}_v(f+f_0))+(\hat{i}_j(f-f_0)+\hat{i}_j(f+f_0))+(\hat{i}_a(f-f_0)+\hat{i}_a(f+f_0))+I_{dc}(\delta(f-f_0)+\delta(f+f_0)) \\ &\quad + I_{dc}(\hat{\eta}(f-f_0)+\hat{\eta}(f+f_0))+I_{ac}\frac{1}{2}(\hat{\eta}(f-2f_0)+\hat{\eta}(f+2f_0))+I_{ac}\frac{1}{2}(\delta(f-2f_0)+\delta(f+2f_0)). \end{aligned} \tag{E3}$$

We obtain the PSD in the usual way by multiplying Eq. (E3) with its complex conjugate. The PSD will contain auto-correlation and cross correlation terms. For the latter, we can find, on the one hand, cross correlation terms between different quantities, which vanish since they are completely uncorrelated. On the other hand, there are also cross correlation terms of the same quantity shifted by different frequencies. Those terms may not vanish since some physical processes can lead to the appearance of harmonics. However, in the following, we will also assume that these terms vanish. This is a good approximation if we choose f_0 and $2f_0$ to be away from mechanical and electronic resonances in the system. We are then only left with the auto-correlation terms. We have

$$\begin{aligned} S'_{t,ac} &= I_{ac}^2 S'_\eta(f)+(S'_v(f-f_0)+S'_v(f+f_0)) \\ &\quad + (S'_j(f-f_0)+S'_j(f+f_0))+(S'_a(f-f_0)+S'_a(f+f_0)) \\ &\quad + I_{dc}^2(\delta(f-f_0)+\delta(f+f_0))+I_{dc}^2(S'_\eta(f-f_0)+S'_\eta(f+f_0)) \\ &\quad + I_{ac}^2\frac{1}{4}(S'_\eta(f-2f_0)+S'_\eta(f+2f_0)) \\ &\quad + I_{ac}^2\frac{1}{4}(\delta(f-2f_0)+\delta(f+2f_0)). \end{aligned} \tag{E4}$$

Note that the S' denotes the PSD defined for frequencies in $(-\infty,\infty)$. In the derivation of the noise for the dc mode, we used the PSD defined on the one-sided range $[0,\infty)$, which is two times the two-sided PSD at finite frequencies. We can see that the power spectral densities occurring in Eq. (E4) are shifted by the frequencies $\pm f_0$ or $\pm 2f_0$. If the noise is only due to Gaussian white noise, the PSD will be constant and the frequency shifts do not matter. On the other hand, $1/f$ noise will be shifted away from zero frequency to f_0. Any contribution near f_0 will be shifted to near zero frequency by the demodulation. The lock-in is followed by a low-pass filter with the transfer function $H(f)$. The noise power of the lock-in output is calculated to be

$$P_{noise} = \int_{-\infty}^{\infty} S'(f)|H(f)|^2 df. \tag{E5}$$

Let us first examine the contributions of the delta functions to the noise power,

$$P_{noise,\delta} = \int_{-\infty}^{\infty}[\delta(f-f_0)+\delta(f+f_0)]|H(f)|^2 df = 2|H(f_0)|^2. \tag{E6}$$

The result shows that the noise at the frequency component of f_0 can be effectively suppressed by using the low-pass filter. We can also see that we can restrict the integration to the positive frequency range and double the integral, thereby going to a one-sided representation of the PSD. Analogously, we can determine the contribution of the other terms to the noise power,

$$
\begin{aligned}
P_{noise,f_0} &= \int_{-\infty}^{\infty} [S'(f - f_0) + S'(f + f_0)]|H(f)|^2 df \\
&= \int_{-\infty}^{\infty} S'(f)\big(|H(f - f_0)|^2 + |H(f + f_0)|^2\big) df \\
&= 2\int_{-\infty}^{\infty} S'(f)|H(f - f_0)|^2 df \\
&= \int_{0}^{\infty} S(f)|H(f - f_0)|^2 df. \qquad \text{(E7)}
\end{aligned}
$$

In the calculation, we first shifted the integration for the two PSD, resulting in two shifted transfer functions of the filter. Since the PSD and filter transfer function are symmetric with respect to their centers, we used only one integrand and doubled its value. The doubled two-sided PSD $2S'$ we denote as the one-sided PSD S. Finally, we note that the bandwidth of the filter transfer function $H(f - f_0)$ is sufficiently narrow around f_0 such that we can restrict the integration to the positive frequency side. Thereby, we recover the noise power calculation as for the dc mode, however, with a shifted transfer function of the filter. The total PSD of the ac mode for positive frequencies now follows directly and is defined in the main text in Eq. (17).

REFERENCES

1. G. E. Moore, "Cramming more components onto integrated circuits," Proc. IEEE **86**, 82–85 (1998).
2. J. Homoth, M. Wenderoth, T. Druga, L. Winking, R. G. Ulbrich, C. A. Bobisch, B. Weyers, A. Bannani, E. Zubkov, A. M. Bernhart, M. R. Kaspers, and R. Möller, "Electronic transport on the nanoscale: Ballistic transmission and Ohm's law," Nano Lett. **9**, 1588–1592 (2009).
3. B. Voigtländer, V. Cherepanov, and P. Coenen, "The multimeter at the nanoscale," Vak. Forsch. Prax. **28**, 38–42 (2016).
4. P. Willke, M. A. Schneider, and M. Wenderoth, "Electronic transport properties of 1D-defects in graphene and other 2D-systems," Ann. Phys. **529**, 1700003 (2017).
5. P. Muralt and D. W. Pohl, "Scanning tunneling potentiometry," Appl. Phys. Lett. **48**, 514–516 (1986).
6. J. P. Pelz and R. H. Koch, "Extremely low-noise potentiometry with a scanning tunneling microscope," Rev. Sci. Instrum. **60**, 301–305 (1989).
7. M. Rozler and M. R. Beasley, "Design and performance of a practical variable-temperature scanning tunneling potentiometry system," Rev. Sci. Instrum. **79**, 073904 (2008).
8. T. Druga, M. Wenderoth, J. Homoth, M. A. Schneider, and R. G. Ulbrich, "A versatile high resolution scanning tunneling potentiometry implementation," Rev. Sci. Instrum. **81**, 083704 (2010).
9. A. Bannani, C. A. Bobisch, and R. Möller, "Local potentiometry using a multiprobe scanning tunneling microscope," Rev. Sci. Instrum. **79**, 083704 (2008).
10. S.-H. Ji, J. B. Hannon, R. M. Tromp, V. Perebeinos, J. Tersoff, and F. M. Ross, "Atomic-scale transport in epitaxial graphene," Nat. Mater. **11**, 114 (2011).
11. F. Lüpke, S. Korte, V. Cherepanov, and B. Voigtländer, "Scanning tunneling potentiometry implemented into a multi-tip setup by software," Rev. Sci. Instrum. **86**, 123701 (2015).
12. W. Zwerger, L. Bönig, and K. Schönhammer, "Exact scattering theory for the Landauer residual-resistivity dipole," Phys. Rev. B **43**, 6434–6439 (1991).
13. C. S. Chu and R. S. Sorbello, "Phase-sensitive scanning tunneling potentiometry and the local transport field in mesoscopic systems," Phys. Rev. B **42**, 4928–4939 (1990).
14. J.-S. Wu and M. M. Fogler, "Scattering of two-dimensional massless Dirac electrons by a circular potential barrier," Phys. Rev. B **90**, 235402 (2014).
15. B. G. Briner, R. M. Feenstra, T. P. Chin, and J. M. Woodall, "Local transport properties of thin bismuth films studied by scanning tunneling potentiometry," Phys. Rev. B **54**, R5283–R5286 (1996).
16. R. Möller, C. Baur, A. Esslinger, and P. Kürz, "Scanning noise potentiometry," J. Vac. Sci. Technol. B **9**, 609–611 (1991).
17. B. Koslowski and C. Baur, "New potentiometry method in scanning tunneling microscopy: Exploiting the correlation of fluctuations," J. Appl. Phys. **77**, 28–33 (1995).
18. J. M. R. Weaver and D. W. Abraham, "High resolution atomic force microscopy potentiometry," J. Vac. Sci. Technol. B **9**, 1559–1561 (1991).
19. A. De Cecco, V. S. Prudkovskiy, D. Wander, R. Ganguly, C. Berger, W. A. de Heer, H. Courtois, and C. B. Winkelmann, "Non-invasive nanoscale potentiometry and ballistic transport in epigraphene nanoribbons," Nano Lett. **20**, 3786–3790 (2020).
20. J.-F. Ge, M. Ovadia, and J. E. Hoffman, "Achieving low noise in scanning tunneling spectroscopy," Rev. Sci. Instrum. **90**, 101401 (2019).
21. J. A. Støvneng and P. Lipavský, "Thermopower in scanning-tunneling-microscope experiments," Phys. Rev. B **42**, 9214–9216 (1990).
22. T. Druga, "Graphen auf Siliziumcarbid: elektronische Eigenschaften und Ladungstransport," Ph.D. thesis, Georg-August-Universität Göttingen, 2014, available at https://ediss.uni-goettingen.de/handle/11858/00-1735-0000-0022-5EDC-1.
23. R. M. Feenstra and B. G. Briner, "The search for residual resistivity dipoles by scanning tunneling potentiometry," Superlattices Microstruct. **23**, 699–709 (1998).
24. W. Wang, K. Munakata, M. Rozler, and M. R. Beasley, "Local transport measurements at mesoscopic length scales using scanning tunneling potentiometry," Phys. Rev. Lett. **110**, 236802 (2013).
25. P. Willke, T. Druga, R. G. Ulbrich, M. A. Schneider, and M. Wenderoth, "Spatial extent of a Landauer residual-resistivity dipole in graphene quantified by scanning tunnelling potentiometry," Nat. Commun. **6**, 6399 (2015).
26. P. Willke, T. Kotzott, T. Pruschke, and M. Wenderoth, "Magnetotransport on the nano scale," Nat. Commun. **8**, 15283 (2017).
27. A. Sinterhauf, G. A. Traeger, D. Momeni Pakdehi, P. Schädlich, P. Willke, F. Speck, T. Seyller, C. Tegenkamp, K. Pierz, H. W. Schumacher, and M. Wenderoth, "Substrate induced nanoscale resistance variation in epitaxial graphene," Nat. Commun. **11**, 555 (2020).
28. Q. Wang, W. Zhang, L. Wang, K. He, X. Ma, and Q. Xue, "Large-scale uniform bilayer graphene prepared by vacuum graphitization of 6H-SiC(0001) substrates," J. Phys.: Condens. Matter **25**, 095002 (2013).
29. D. Huang, S. Liu, I. Zeljkovic, J. F. Mitchell, and J. E. Hoffman, "Etching of Cr tips for scanning tunneling microscopy of cleavable oxides," Rev. Sci. Instrum. **88**, 023705 (2017).
30. L.-J. Yin, H. Jiang, J.-B. Qiao, and L. He, "Direct imaging of topological edge states at a bilayer graphene domain wall," Nat. Commun. **7**, 11760 (2016).
31. O. S. Lumbroso, L. Simine, A. Nitzan, D. Segal, and O. Tal, "Electronic noise due to temperature differences in atomic-scale junctions," Nature **562**, 240–244 (2018).